

POLITECNICO DI TORINO

Master's Degree in Mechanical Engineering



Master's Degree Thesis

Global/local analysis of variable stiffness composite laminates

Supervisors

Prof. Erasmo CARRERA

Prof. Alfonso PAGANI

Prof. Riccardo AUGELLO

Prof. Alberto RACIONERO

Candidate

Tommy Kenzo MIURA

APRIL 2023

Abstract

The present work aims to provide a framework using software tools that enable the global-local, finite element analysis of Variable Angle Tow composites. The workflow proposes using 2D plate elements for a global simulation, and the subsequent use of a local analysis to obtain accurate results in the thickness of the material. The global model has its foundation in Equivalent Single layer and Plate Theory adapted for VAT laminates. It is built with square finite elements with four nodes and one Gaussian point in its center, where the tow angle and its general properties are calculated. The local model is instead based on the Carrera Unified Formulation and uses third-degree Lagrangian polynomial to interpolate the displacements and rotations of the global model. This type of analysis is implemented using the commercial software FEMAP/NASTRAN for the computations on the global model and the in-house software MUL2@GL plug-in developed by the MUL2 lab of Politecnico di Torino for the local one. The capabilities of the workflow are put into test analyzing a thin and a thick plate under bending and a third thin one under stretching. The final computation of the laminar and interlaminar stresses is compared to results in the literature and other Layerwise models to validate the global-local workflow.

Keywords: VAT; Global-Local analysis; Carrera Unified Formulation.

Table of Contents

List of Figures	IV
1 Introduction	1
1.1 Classical Composites	3
1.2 Variable Stiffness Laminates	5
1.3 Global-local Method	7
1.4 Motivation	8
2 Variable Angle Tow Laminates	10
2.1 Manufacturing	10
2.1.1 Tailored Fiber Placement (TFP)	11
2.1.2 Automated Fiber Placement (AFP)	13
2.1.3 Continuous Tow Shearing (CTS)	15
3 Unified Finite Elements	19
3.1 Reference Systems	20
3.1.1 Global Reference System	20
3.1.2 Fiber Reference System	21
3.2 Geometrical Relations	22
3.3 Equilibrium Equations	23
3.4 Boundary Conditions	24
3.5 Constitutive Equations	24
3.6 Governing Equations	26
3.6.1 Principle of Virtual Displacements: Strong Form	27
3.6.2 Principle of Virtual Displacements: Weak Form	29
3.7 Introduction to FEM	30
3.8 Equivalent Single Layer and Layerwise Methods	31
3.9 Global Model FEM	32
3.9.1 Governing Equations for Thin Plates under Bending	32
3.9.2 FEM for Thin Plates under Bending	34
3.10 Local Model FEM	36

3.10.1	Carrera Unified Formulation	37
3.10.2	Local FEM with CUF	39
4	Global-Local Approach	41
4.1	Global-Local Methodology	41
4.2	The splines method	42
4.2.1	Limitations	43
4.3	The API program	45
4.3.1	Introduction to the API	45
4.3.2	Breakdown of the program	45
4.4	The Local Model	46
5	Numerical Results	48
5.1	Thin Plate Bending	48
5.1.1	FEM Model	49
5.1.2	Mesh Convergences	50
5.1.3	Results Comparison	53
5.1.4	Patch-wise Improvement	56
5.1.5	Summary of the Thin Plate Bending	59
5.2	Thick Plate Bending	59
5.2.1	FEM Model	59
5.2.2	Mesh Convergences	60
5.2.3	Results Comparison	66
5.2.4	Patchwise Improvement	68
5.2.5	Summary of the Thick Plate Bending	68
5.3	Thin Plate Stretching	70
5.3.1	FEM Model	70
5.3.2	Mesh Convergences	71
5.3.3	Results Comparison	73
5.3.4	Patch-wise Improvement	77
5.3.5	Summary of the Thin Plate Stretching	80
6	Conclusions	81
A	Cubic Interpolations of the Local CUF Element	83
	Bibliography	85

List of Figures

1.1	Share of composite components in aircraft	1
1.2	Asia Pacific market size	2
1.3	Market composition by application	2
1.4	Forecast of the number of flights from 2017 to 2040	3
1.5	Mechanical properties of mild steel compared to composites	4
1.6	Fiber reinforced composite types	5
1.7	Particulate reinforced composite types	5
1.8	Classical 45° straight fiber vs VAT laminate	6
1.9	Local models for a plate with a cutout	8
2.1	Sketch of the TFP process	11
2.2	TFP machine sewing the roving of carbon fiber	12
2.3	Final TFP component after impregnation	12
2.4	Simplified sketch of an AFP head working	13
2.5	Layup of a cryogenic tank and a blended wing body	14
2.6	Gaps and overlaps due to small turning radius	15
2.7	Ply staggering sketch	16
2.8	Wrinkling caused in TFP process	16
2.9	Resin rich area in laminate	17
2.10	Fiber discontinuity caused during AFP process	17
2.11	Sketch of a CTS machine head placing a tow	18
3.1	Representation of a generic 3D body	20
3.2	Graphical representation of Cauchy’s second-order stress tensor	21
3.3	Reference system used in a VAT laminate path	22
3.4	Plane domain discretized into triangular elements	31
3.5	Comparison between the stiffness matrices of ESL and LW methods	32
3.6	Graphical Representation of the local CUF element	36
3.7	Graphical Representation of the local CUF element	37
3.8	Notation used to define the top and bottom surfaces of a plate	38

4.1	Global-Local methodology diagram	42
4.2	Square plate with 1-meter side	43
4.3	Spline definition for the fiber orientation	43
4.4	Square plate with 1-meter side	44
4.5	Approximation error of the splines	44
4.6	Diagram of the whole API program	46
4.7	CQUAD4 element nodes indexing	46
5.1	Thin Plate under Bending	49
5.2	Thin Plate layup and fiber orientation	50
5.3	Thin Plate Bending - General material properties	50
5.4	Thin Plate Bending - Global Convergence u_z	51
5.5	Thin Plate Bending - Local In-plane Convergence Comparison . . .	52
5.6	Thin Plate Bending - Local Out-of-plane Convergence Comparison .	52
5.7	EW Stress σ_{xx} at Q	54
5.8	EW Stress σ_{yy} at Q	54
5.9	EW Stress σ_{xy} at Q	54
5.10	EW Stress σ_{xz} at Q	55
5.11	EW Stress σ_{yz} at Q	55
5.12	EW Stress σ_{xx} at C	55
5.13	EW Stress σ_{yy} at C	55
5.14	EW Stress σ_{xy} at C	55
5.15	PW Stress σ_{xx} at Q	57
5.16	PW Stress σ_{yy} at Q	57
5.17	PW Stress σ_{xy} at Q	57
5.18	PW Stress σ_{xz} at Q	57
5.19	PW Stress σ_{yz} at Q	57
5.20	PW Stress σ_{xx} at C	58
5.21	PW Stress σ_{yy} at C	58
5.22	PW Stress σ_{xy} at C	58
5.23	Thick Plate under Bending	60
5.24	Thick Plate layup and fiber orientation	61
5.25	General material properties of the Thick Plate	61
5.26	Thick Plate Bending - Global Convergence	62
5.27	Thick Plate Bending - Local In-plane Convergence Comparison . . .	62
5.28	Thick Plate Bending - Local In-plane Convergence	63
5.29	Thick Plate Bending - Local Convergence Comparison	64
5.30	Thick Plate Bending - Local Convergence Comparison	65
5.31	Thin Plate Bending - Local Out-of-plane Convergence Comparison .	65
5.32	Comparison of vertical displacements	66
5.33	EW Stress σ_{xx} at Q	67

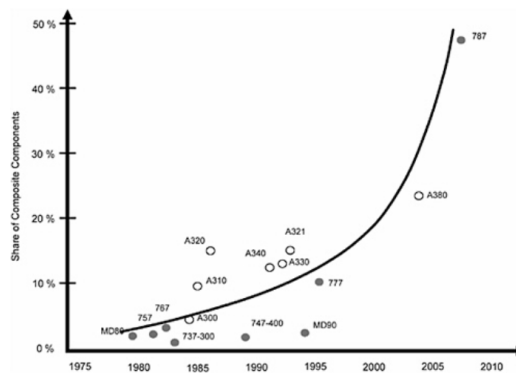
5.34	EW Stress σ_{yy} at Q	67
5.35	EW Stress σ_{xy} at Q	67
5.36	EW Stress σ_{xz} at Q	67
5.37	EW Stress σ_{yz} at Q	67
5.38	PW Stress σ_{xx} at Q	69
5.39	PW Stress σ_{yy} at Q	69
5.40	PW Stress σ_{xy} at Q	69
5.41	PW Stress σ_{xz} at Q	69
5.42	PW Stress σ_{yz} at Q	69
5.43	PW Stress σ_{zz} at Q	69
5.44	Thin Plate under Stretching model	70
5.45	Material properties of the Thin Plate under Stretching	71
5.46	Thin Plate Stretching - Global Convergence u_x	72
5.47	Thin Plate Stretching - Global Convergence u_y	72
5.48	Thin Plate Stretching - Global Convergence u_y	73
5.49	EW Stress σ_{xx} at C	75
5.50	EW Stress σ_{yy} at C	75
5.51	EW Stress σ_{xy} at C	75
5.52	EW Stress σ_{xx} at E	76
5.53	EW Stress σ_{yy} at E	76
5.54	EW Stress σ_{xy} at E	76
5.55	EW Stress σ_{xz} at E	76
5.56	EW Stress σ_{yz} at E	76
5.57	PW Stress σ_{xx} at C	78
5.58	PW Stress σ_{yy} at C	78
5.59	PW Stress σ_{xy} at C	78
5.60	PW Stress σ_{xx} at E	79
5.61	PW Stress σ_{yy} at E	79
5.62	PW Stress σ_{xy} at E	79
5.63	PW Stress σ_{xz} at E	79
5.64	PW Stress σ_{yz} at E	79

Chapter 1

Introduction

The composites material industry has been growing rapidly. According to [1] the global market is expected to surpass US\$128.82 billion in 2028, a growth of 78% in comparison to 2020. This is due to the broad variety of industries investing in this sector. Automotive, transportation, wind energy, aerospace, and defense industries are the main players driving its rapid growth. Special attention must be paid to the aerospace industry, which is one that has had a huge increase in its investments on composites, as can be seen in Figure 1.1. This figure shows the percentage of of composite components in function of the time in years and it becomes evident that the usage of composite materials in an aircraft has followed an exponential rise since the secong half of the last century, which went from around 3% in 1975 to 23% with the Boeing A380 in 2004 and quickly more than doubled to 48% in a matter of 4 years with the construction of the Boeing 787.

Figure 1.1: Share of composite components in aircraft

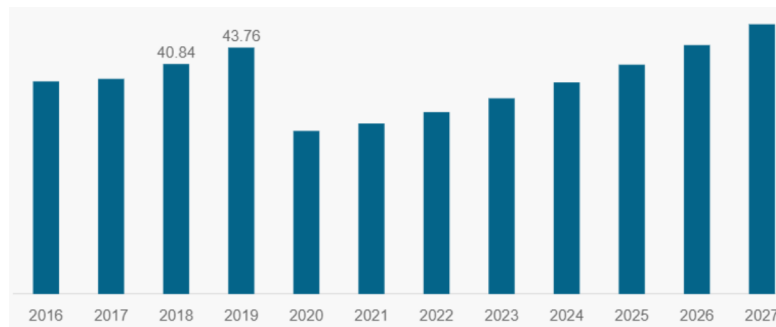


Source: [2]

A more updated study on the composites market size was conducted in 2020 by

[3]. This study corroborates the expectations of [1] that this industry is quickly growing, despite the negative effects of the pandemic. Figure 1.2 shows the Asia Pacific market size of composites in the study period of 2016 to 2027, using 2019 as the reference year. It is possible to see that until the pandemic this market was under fast growth from 2016 to 2019 and suffered from a significant dip of around 20% in a single year, but the estimates show a full recovery in a matter of 5 years and in 2026 the composite market will have outgrown 2019. This represents the continuity and resilience of composites in the Asia Pacific market, which is representative of the general tendencies in the world.

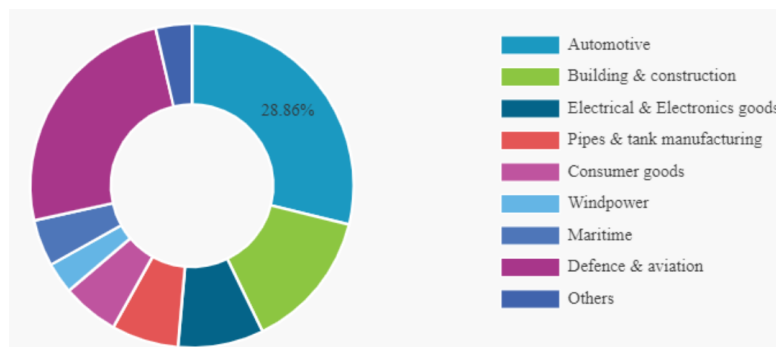
Figure 1.2: Asia Pacific market size



Source: [3]

Once again, in this research, the main players considered in the composite market are the automotive and aviation sectors, which account for more than 50% of the whole market. Figure 1.3 shows the market share of composites by application. Two main conclusions can be drawn from these few studies, the composite materials

Figure 1.3: Market composition by application



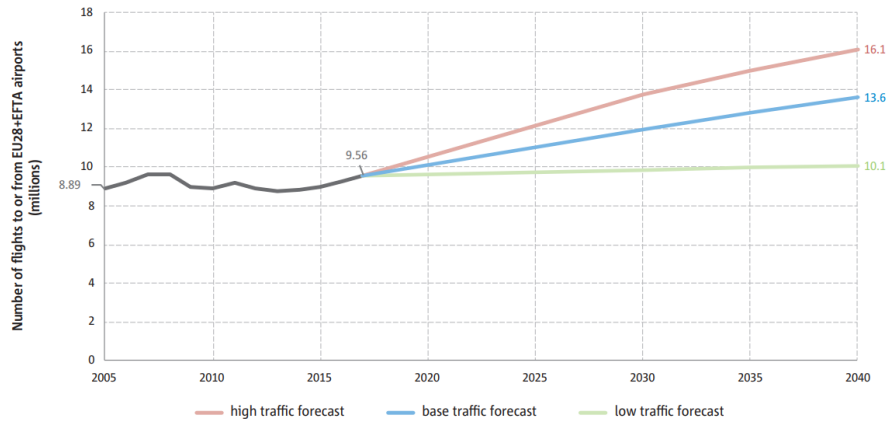
Source: [3]

market is under growth and is expected to continue like this for the next decade.

Within it, the aviation sector is its biggest supporter.

Upon further inspection of aviation tendencies, according to [4] the single largest cost for most aircraft operators, both military and commercial, is fuel. In Europe, for the year 2017, the average fuel consumption per passenger was 24% lower than in 2005, but the total air traffic grew by almost 60% for this period leading to an increase in total CO_2 emissions of 16%. Furthermore, this scenario is likely to continue, as Figure 1.4 estimates that the number of flights should increase by 68% optimistically, by 42% on a realistic basis, and by 5.6% in a worst case scenario from 2017 until 2040. It is worth mentioning that this forecast was done prior to the pandemic, but the general increase in air traffic should still happen. As Europe's 2030 agenda for sustainable development directly depend on carbon

Figure 1.4: Forecast of the number of flights from 2017 to 2040



Source: [4]

dioxide emissions, more technological developments must be achieved to guarantee an improvement in aircrafts's fuel economy so that a significant increase in number of flights does not cause a simultaneous rise of emissions.

1.1 Classical Composites

From an engineering point of view, the composite material class is second only to the steel class, when it comes to industrial significance and range of applications. According to [5], which is due to the versatility of mechanical properties that this class possesses. The main reason composite materials receive so much attention is on account of their higher Young's modulus, higher tensile strength, and lower density when compared to some steel alloys. Even though the data are only approximate, Figure 1.5 shows the benefits that carbon fiber composites may have

with respect to mild steel, at least when it comes to higher Young's modulus and lower density. This potential of producing stiff and lightweight structures is what aircraft and automotive manufacturers try to exploit to achieve optimal and fuel-efficient vehicles.

Figure 1.5: Mechanical properties of mild steel compared to composites

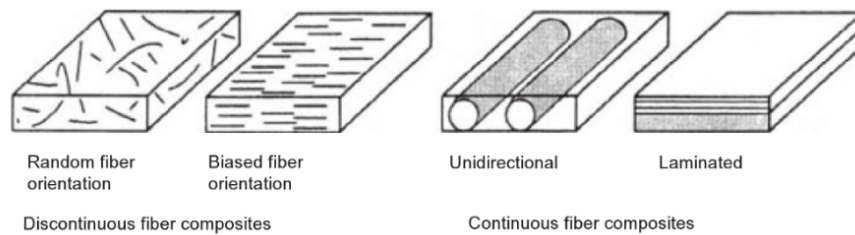
Material	Density ρ (kg m ⁻³)	Young's modulus E (GPa)	Tensile strength σ_s (MPa)	Fracture energy G_c (kJ m ⁻²)	Thermal conductivity K (W m ⁻¹ K ⁻¹)	Thermal expansivity α ($\mu\epsilon$ K ⁻¹)
Mild steel	7800	208	400	100	40	17
Concrete	2400	40	20	0.01	2	12
Spruce (<i>//</i> to grain)	600	16	80	4	0.5	3
Spruce (\perp to grain)	600	1	2	0.2	0.3	10
Chopped strand mat (in-plane)	1800	20	300	30	8	20
Carbon fibre composite (<i>//</i> to fibres)	1600	200	1500	10	10	0
Carbon fibre composite (\perp to fibres)	1600	10	40	0.2	2	30
Al-20% SiC _p (MMC)	2800	90	300	2	140	18

Source: [5]

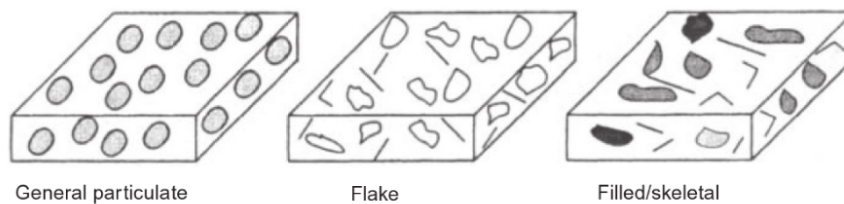
Composite materials are usually categorized accordingly to the type of their reinforcements, [6]:

- Fibrous: the reinforcement has the shape of fibers, which can be long, having a very high length-to-diameter ratio, or short (whiskers), with a length-to-diameter ratio between 5 and 1000.
- Particulate: the reinforcements may be of any shape or configuration. Particulate reinforcements are divided into flakes and filled.

Within these two types of reinforcements, it is also possible for them to be produced in various manners, which alter their mechanical properties, possibly making them isotropic, anisotropic, or orthotropic. Fibrous reinforcements can be discontinuous or continuous and continuous fibrous reinforcements can be single-layered, multilayered, or even have random or biased orientation, as shown in Figure 1.6. Particulate composites, on the other hand, are usually randomly dispersed in the matrix, constituting isotropic composites. Figure 1.7 shows the types of particulate reinforcements:

Figure 1.6: Fiber reinforced composite types

Source: [6]

Figure 1.7: Particulate reinforced composite types

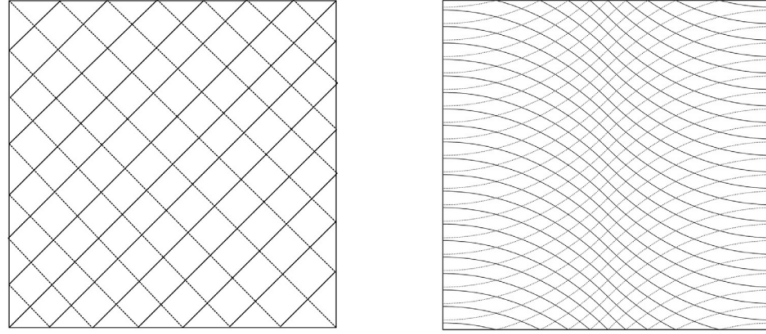
Source: [6]

1.2 Variable Stiffness Laminates

The most recent developments in technology and manufacturing show a tendency towards the study of variable stiffness laminates. This is not by chance, in practical applications, VS laminates are an optimized version of traditional fiber-reinforced composites. As the name suggests, their distinct characteristic is the local variation of their stiffness, which allows manufacturers to choose which regions of the material should be stiffer or more compliant according to their project's design and requirements, which makes it possible to build even lighter parts while maintaining its structural integrity. Currently, there are many ways to make a laminate have inhomogeneous stiffness:

- Variation of the fiber volume fraction, as presented in the work of [7]
- Local variation of the number of plies in the laminate, as described by [8]
- Variation of the path of fibers in the matrix, as studied by [9]

Out of those methods, the one that is the most interesting is the third. Laminates that have a variable fiber path, as opposed to straight, are called Variable Angle Tow (VAT). Figure 1.8 shows the fiber paths of a classical laminate on the left and the similar fiber paths on a VAT on the right.

Figure 1.8: Classical 45° straight fiber vs VAT laminate

Source: [10]

This capability of customizing the stiffness of your base material by producing fiber paths that follow curvilinear trajectories brings many new challenges to structural analysis and manufacturing and currently, there are many works that are aimed toward a better comprehension of these structures' behavior such as the work of [11] that uses a Rayleigh-Ritz approach to determine the prebuckling load distributions and critical buckling load of VAT plates providing a more efficient way to evaluate the buckling load of VAT laminates when compared to other numerical solutions as well as the work of [12] that uses the Hellinger-Reissner principle to obtain a mixed quadrilateral 3D finite element that can better simulate the buckling behavior of VAT. The work of [13] complements the previous one by adding a semi-analytical formulation based on a variational approach to solve the post-buckling problem in VAT plates. Then [14] adds to the instability problem by using Bolotin's method to study the influences of the fiber towpath and periodical compressive loads.

Some works also introduce manufacturing defects in their simulations. The work of [15] developed a computer-aided modeling tool for VAT laminates manufactured by the CTS technique to provide a convenient way to create an ABAQUS finite element model of this type of composite with non-linear fiber angle variation that cannot be formulated mathematically. Then there is the article of [16], which uses higher-order shear deformation theories on moderately-thick plates laminates that present gaps and overlaps due to the AFP process. To complement the numerical simulations of defects, the work of [10] introduces a stochastic approach to study the influence of misalignments in fiber placement and analyze the stress and failure indexes distribution caused by random defects on VAT laminates. Then [17] investigates the uncertainty of the winding angle in cylindrical shells while also considering the thickness variation due to overlaps.

Another set of studies worth mentioning is those that use the Carrera Unified

Formulation (CUF). The work of [18] proposes an improvement on the dynamic response of complex aeronautical structures composed by VAT laminates through the use of the Carrera Unified Formulation and refined kinematic structural models. This study also investigates the effect of different fiber paths on the performance of wing structures. Complementing his own work, [19] presents a refined beam model based on CUF to analyze the free vibration of VAT laminates. Another interesting numerical approach similar to the one developed in this thesis is the work of [20] that uses CUF to determine the buckling loads and natural frequencies in VAT square plates by using the layerwise theory. Then it runs a genetic algorithm optimization method to maximize the first critical buckling load and the first natural frequency using the definition of linear fiber orientation angles.

Furthermore, there are works that consider hygrothermal loads, such as the work of [21] proposes a novel semi-analytical methodology to conduct hygrothermomechanical analysis on thin to relatively-thick fiber-steered conical and cylindrical composite panels. Also, [22] studies the thermal flutter characteristics of an infinitely long VAT composite curved panel in supersonic airflow.

1.3 Global-local Method

When it comes to simulation, the Finite Element Analysis is one of the most used tools to evaluate structural integrity and a component's characteristics, but depending on the geometrical or material characteristics of each analysis, it can require large amounts of computational time and effort. This is especially true regarding VAT components because their plate geometry is such that their length and width are usually 100 times larger than their thickness, which requires a very fine mesh to obtain accurate results. To put things into perspective, composite plates usually need very few 2D elements for buckling and modal analyses, which is highly computationally affordable, but this type of elements does not allow the computation of zig-zag and free-edge effects, which would require the use of 3D elements as they need a tridimensional stress state to be calculated. According to [23], a 1-meter length square plate would require around 10^9 elements to be correctly discretized as at least 3 elements are necessary along the thickness of the plate.

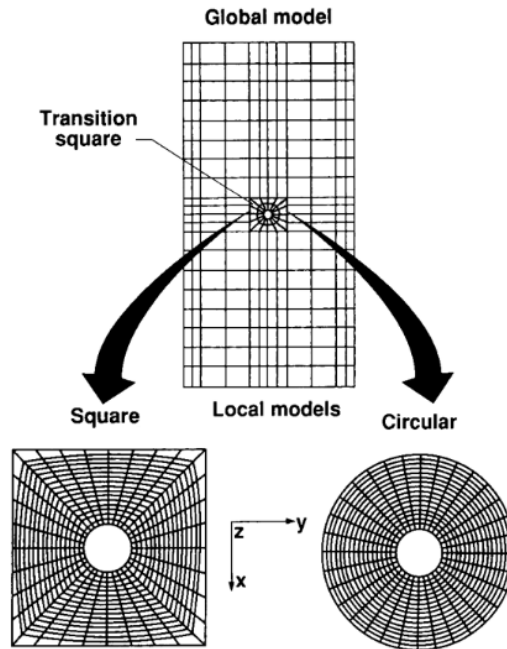
This is where the Global-Local (GL) method becomes most useful. It saves computational effort by making the heaviest calculations only at the desired locations, usually near cutouts, contacts, corners, or virtually any regions that have a steep stress gradient and require finer meshes. Currently, there are 3 main forms through which this method is applied:

1. **Local mesh refinement.** The global model is composed of a coarse mesh and, for the critical regions, a much finer mesh is used. In Figure 1.9 a global

model of a rectangular-shaped plate with a small hole in its center can be seen as well as two types of local refinement, a square local model on the left and a circular one on the right.

2. **Multi-model.** As the name suggests, this method takes advantage of different mathematical models for each region of interest. It requires special attention to the displacement and stresses coupling at the interface of the models.
3. **Superelements.** It is a grouping of finite elements that meet certain criteria and, when assembled, can be regarded as one for computational purposes ([24]).

Figure 1.9: Local models for a plate with a cutout



Source: [25]

In this work, the second method is chosen as it is particularly interesting for calculating the interlaminar stresses in VAT components because it completely avoids them in unnecessary regions.

1.4 Motivation

The motivation for the development of this work needs to be explained from a big picture. Shortly put, composite materials, especially laminates have a huge

potential in comparison to the traditional metallics. As technology and science improves, manufacturing methods follow, enabling the usage of better and lighter materials. The economic tendencies show that, in general, automotive and aircraft industries are driving the growth of the composites industry to improve their own products. This drives the development of scientific publications and studies in this sector. This paper lies within this general context.

In a more focused academic picture, there are many works that have been published that study the behavior of VAT laminates and many works that use the Global-Local analysis to obtain precise results while maintaining computational efforts at a reasonable threshold, however to the best of the author's knowledge, there aren't papers that propose a global-local analysis of VAT composites. The vast majority of studies that propose a method to analyze the behavior of VAT laminates use 3D elements to obtain their results, which may become quite time-consuming for large or more complex multiple-layered structures. For this reason, this work proposes a simplified approach that does not compromise the accuracy. By using the GL method to evaluate the regions of interest in a 2D VAT panel a lot of computational effort might be saved. The main idea is that the Global model is made using 2D elements and for the more critical regions of the laminate, a Local model can be made to evaluate the through-the-thickness stresses, making more optimized use of computational effort.

Chapter 2

Variable Angle Tow Laminates

In general, the mechanical behavior of materials display a dependency on their manufacturing process. This is specially true when dealing with Variable Angle Tow laminates. As its name makes it clear, these are composites that have their fibers aligned upon a custom path, enabling the designers to tailor components for each engineering scenario. This high level of parts customization creates a necessity to understand and control the manufacturing of VAT laminates in a way that their mechanical properties can be consistently maintained through production.

This chapter presents a description of how VAT laminates are manufactured and then simulated. A presentation of the main processes is necessary, since the mechanical performance of VAT panels also depends on the type of process chosen and the techniques adopted within it.

2.1 Manufacturing

Historically, manufacturing technologies are what limit the production of any component or structure. It is one challenge to conceive a new type of material and produce a functioning prototype, but it is another one to mass produce and make it available to an entire industry. This has been no different for VAT laminates. Even though carbon fiber tapes and meshes have been available for commercial use since 1966 ([26]), the automation and the capability of having fibers follow a custom curvilinear path within the matrix material have significantly matured in recent years with the advent of robot-assisted composite manufacturing that enabled the steering of fibers in the lamina plane. These relatively new technologies are capable of fabricating high-quality large composite components with point-wise variations in stiffness using continuously varying fiber angles, which allow the fabrication of

VAT laminates.

Currently, there are three main manufacturing technologies for fiber placement:

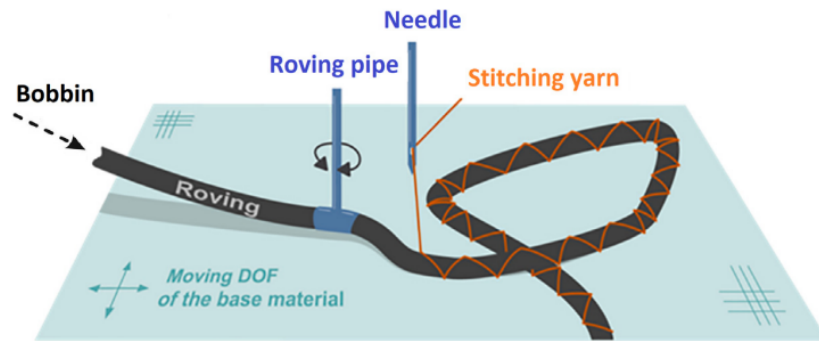
1. Tailored Fiber Placement (TFP);
2. Automated Fiber Placement (AFP);
3. Continuous Tow Placement (CTS).

Each with its own specific models and defects.

2.1.1 Tailored Fiber Placement (TFP)

Tailored Fiber Placement is an embroidery-based tow-steering process that sews a single continuous fiber roving onto a flat textile base material with a stitching yarn. Figure 2.1 shows a sketch of the TFP process and Figure 2.2 shows the real machine while it sews the roving in a zig-zag-like pattern.

Figure 2.1: Sketch of the TFP process



Source: [27]

Usually, this technique is referred to as dry tow placement due to the non-impregnated placement of the fibers. Only after the preformed has taken shape, it is impregnated with resin to form the final component, which has the advantage of being very close to its final form. Before the use of dry fibers, many techniques used pre-impregnated fiber bundles, but it required the use of tape to fix the bundles in place, which led to a decreased flexibility of design. Figure 2.3 shows the final impregnated component sewed in Figure 2.2.

According to [27], TFP has several advantages over AFP and CTS:

1. Possibility to deposit the fiber roving with small radii;
2. Considerable design freedom in terms of the towpath;

Figure 2.2: TFP machine sewing the roving of carbon fiber



Source: [28]

Figure 2.3: Final TFP component after impregnation



Source: [28]

3. Outstanding out-of-plane mechanical performance;
4. Higher tow deposition speed.

[29] also estimated through the use of Finite Element Analysis that the ultimate load was 55% higher for TFP-manufactured VAT plates in comparison to unidirectional notched ones. This result was later validated by tensile loading tests.

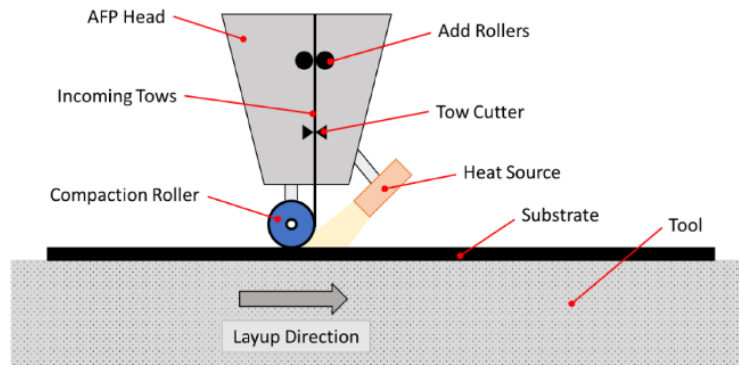
The main defects present in TFP technologies are related to their manufacturing peculiarities. For instance, if the tension of the stitching yarn is too high, the tows will suffer from out-of-plane bucking, or if the tension is too low the fibers will not be correctly restrained against the substrate, and they may move. The defect that may happen more frequently is resin gaps, which are primarily due to the pulling of the tow towards the origin of the curvature. To avoid this defect manufacturers must include a slight overlap of rovings when preparing the machine.

2.1.2 Automated Fiber Placement (AFP)

Automatic Fiber Placement is the most studied method out of the main three. It combines the advantages of tape laying with filament winding to produce high-quality fiber-steered structures with customized local stiffness variations. Also known as Automated Fiber Placement (ATP), it is capable of placing quite wide fiber tows of around 3 to 13 millimeters, continuously, while varying the fiber angles. Its development started around the decade 1980, but it has only significantly matured in recent years, more specifically when the airplane industry started to invest in this technology. The recent developments in AFP techniques show that it has a very high potential for improvement, hence this method is addressed in this work.

AFP composite manufacturing is usually done with the use of a kind of robotic arm, in which the end effector handles and places the tape on the surface of the mold, which may be flat or a complex geometry with curvatures. Fundamentally, the AFP head pulls the tow from a dry material spool and, with the help of a compaction roller, glues it by pressing onto the mold, while heating it. A simplified sketch of this process can be viewed in Figure 2.4.

Figure 2.4: Simplified sketch of an AFP head working



Source: [30]

The flexibility of the robotic arms makes this technology easy to be implemented in the production of components of very different geometries, for example, on the left side of Figure 2.5 a cryogenic tank is being played, and on the right, a blended wing body.

Every manufacturing process has its defects and AFP is no different. According to [27], it has a few design constraints that weigh on the manufacturability and the quality of the final parts. The most important factors that need to be taken into account are:

Figure 2.5: Layup of a cryogenic tank and a blended wing body

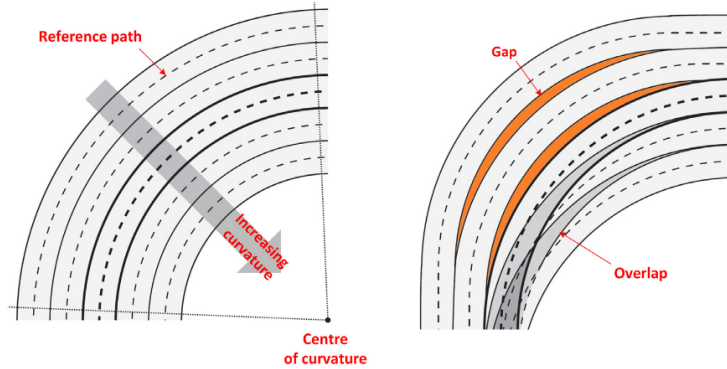


Source: [31]

1. **Minimum cut length.** It is the distance between the contact point to the tow-cutter. Failing to acknowledge its proper design may lead to undesirable gaps in the laminate or ar ply boundaries.
2. **Gaps and overlaps.** The fiber steering procedure itself is prone to gaps, hence to err on the side of caution, manufacturers tend to favor overlaps of tows in the design of their components as they tend to increase the mechanical performance.
3. **Minimum turning radius.** Shown in Figure 2.6. This is essential to take into account. A small turning radius will cause tows to suffer in-plane bending deformations, such as local buckling and thickness change in the inner edge of the tow, which may lead to unpredicted failure. If the turning radius is even smaller, the tow might undergo wrinkling, decreasing even further the strength of the laminate.
4. **Fiber bridging.** If the designer is not careful with the tensile forces pulling the tow, it might detach from the mold surface forming a gap that resembles a bridge.

To avoid these problems, there are some design considerations that can be made, according to the literature:

1. **Tow-overlap.** This technique proposes that a portion of each tow should overlap its neighboring tows to increase the rigidity of the component. This technique has been studied by [11], who found that it increased the buckling load 5 times with respect to a normal straight-fiber composite panel.

Figure 2.6: Gaps and overlaps due to small turning radius

Source: [27]

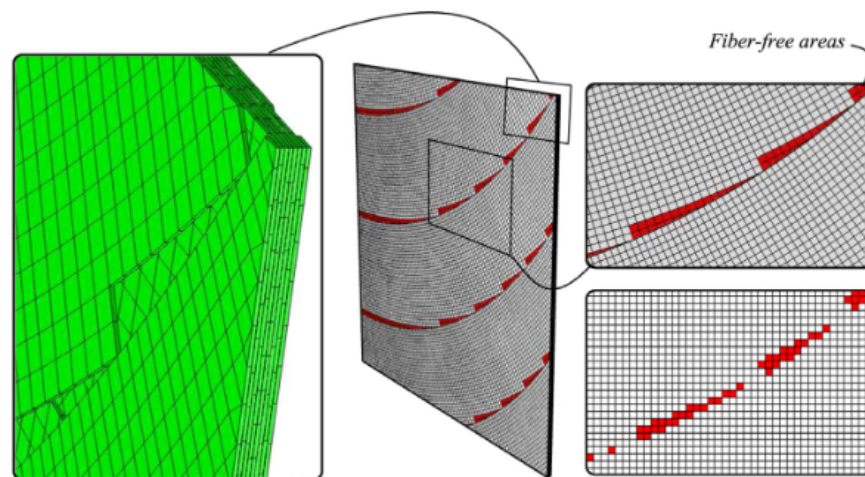
2. **Tow-drop.** The AFP machine is capable of cutting the tow and restarting its placement at another location. Considering this capability, it is possible to program the machine to cut the tow at intersections, creating a constant thickness component. Nevertheless, this generates another problem, in the zones where the tow is cut, there is the formation of small fiber-less regions, which are prone to form resin-rich areas that in turn are critical failure points to consider, as the mechanical properties in this region are much worse.
3. **Ply staggering.** It is very similar to the previous method, it also creates fiber-free regions, but keeps the thickness constant. Its main idea is shifting the path of each ply by a small distance so they do not overlap. This process is better seen in Figure 2.7.

The manufacturing of VAT panels is especially process dependent, the mechanical properties of the final component depend directly on the quality of the methods adopted to lay it. For this reason, many studies also aim to complement their numerical simulations by adding the influence of these process-induced defects. To mention a few, the work of [10] takes into account the inaccuracies of the fiber angles by introducing a stochastic field in them and [32] tries to predict the influence of the tow-drop method, by taking into account resin-rich areas.

2.1.3 Continuous Tow Shearing (CTS)

The Continuous Tow Shearing process was first developed by [33] with the aim of using the shear deformation characteristic of dry tow rather than the in-plane bending deformation used in AFP manufacturing. The first prototype tests showed that this novel method could reduce the process-induced defects of:

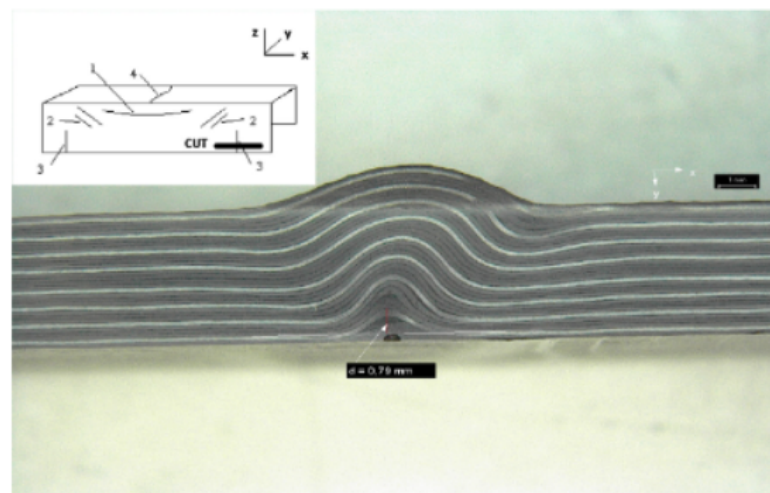
Figure 2.7: Ply staggering sketch



Source: [27]

- Fiber wrinkling, also known as waviness. Represented in Figure 2.8;
- Resin rich areas, shown in Figure 2.9;
- Fiber discontinuities, shown in Figure 2.10.

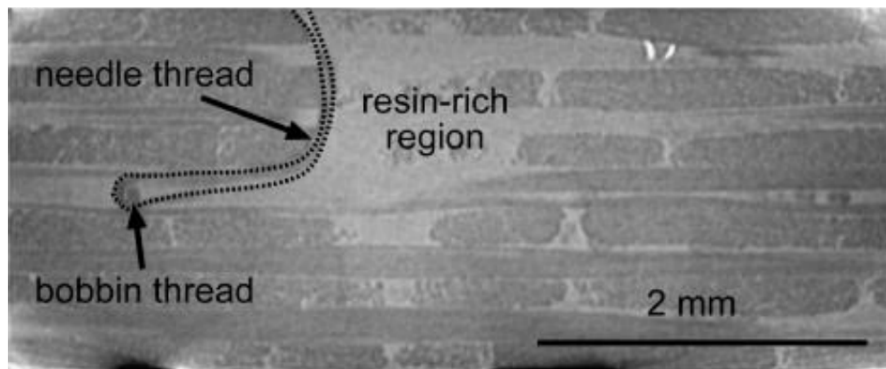
Figure 2.8: Wrinkling caused in TFP process



Source: [34]

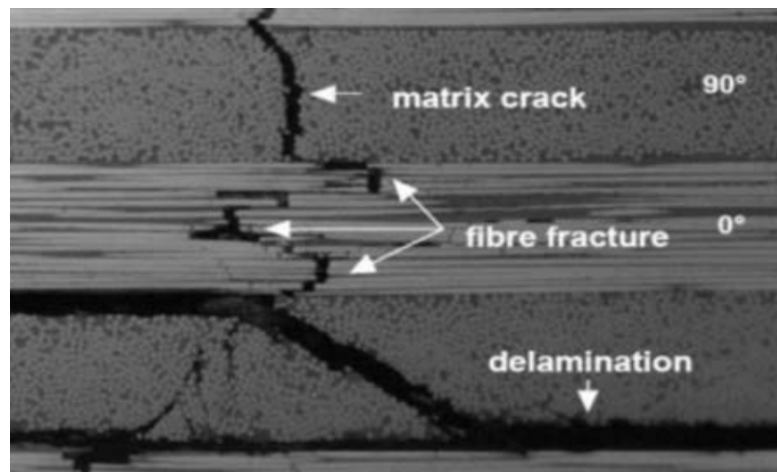
All these benefits arise from the key characteristics of CTS. In this technique, the fiber placement head applies in-plane shear deformation to the dry-tows while they

Figure 2.9: Resin rich area in laminate



Source: [35]

Figure 2.10: Fiber discontinuity caused during AFP process

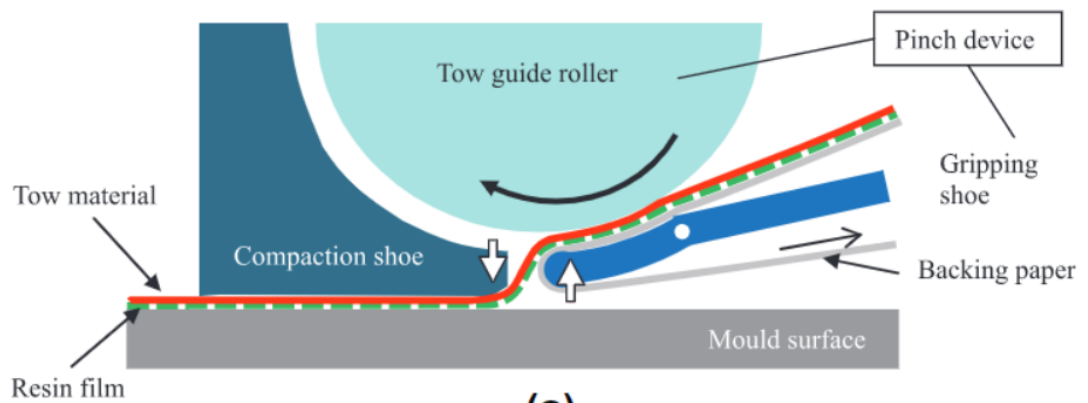


Source: [36]

are placed. To solve the problem of fiber splitting, CTS makes in-situ impregnation, which can eradicate tow gaps or overlaps that appear in the AFP method during the in-plane bending of the tow. This rather novel technology works by pressing a tow of fibers onto a mold surface through the use of a roller and a gripping device that pinches the tow and a compaction shoe that presses it. In Figure 2.11 it is possible to see precisely how the tow undergoes shear deformation right before being attached to the mold.

Even though CTS has some advantages over TFP and AFP methods, it is relatively immature. While these other technologies have had more than 20 years to evolve, CTS has just over a decade of development. Although there are studies of its behavior, the vast majority of publications still only concern AFP technology.

Figure 2.11: Sketch of a CTS machine head placing a tow



(a)
Source: [33]

Chapter 3

Unified Finite Elements

Structural analysis is a field of study in engineering that evaluates the behavior of a solid for a given set of constraints and external loads. Its main objective is usually finding the displacements or the stress state of the structure under review or construction, to estimate whether it can maintain its mechanical integrity during its use. To achieve this objective, an engineer needs to create a model capable of accurately representing the real structure.

All models are always a simplification of reality aiming to simulate the behavior of a structure. They can be often be categorized into two types, analytical or numerical. The first type, albeit able to provide an exact solution to the problem, is impractical for most scenarios. It requires exhaustive mathematical formulation, which often proves to be quite time consuming. Even the representation of a simple two-dimensional plate can prove a challenge in the analytical realm. The latter, numerical models, are built approximately, and can be directly implemented on a computer. These models have the advantage of being versatile, but at the expense of computational effort. Basically, they breakdown a bigger problem into small manageable problems that can be quickly solved by a machine. The most common numerical modeling technique is the Finite Element Method.

The purpose of this chapter is to provide the mathematical premises used in the structural analyses performed in the whole work. It aims to detail the theory behind the construction of the global model and the subsequent local model. It begins by introducing the models that govern the structural behavior of VAT composite plates, which starts with the definition of the coordinate system necessary to define the variable fiber orientation within the material, then it presents the equilibrium equations satisfied for any point in the domain as well as the constitutive equations specific for VAT composites. Next, the governing equations are derived using the Principle of Virtual Displacements (PDV) in its strong form, which is then manipulated to obtain its weak form. Finally, from the previous formulations, it is possible to write the Finite Element Method (FEM) for plates.

The penultimate section of the chapter presents an overview of the two most common methods commercial software use to evaluate layered materials, the Equivalent Single Layer, and the Layerwise methods. Lastly, the final section presents the development of the local model, in which the Carrera Unified Formulation (CUF) is derived from the previously developed PVD to facilitate the coupling between the 2D global model and the 3D local one.

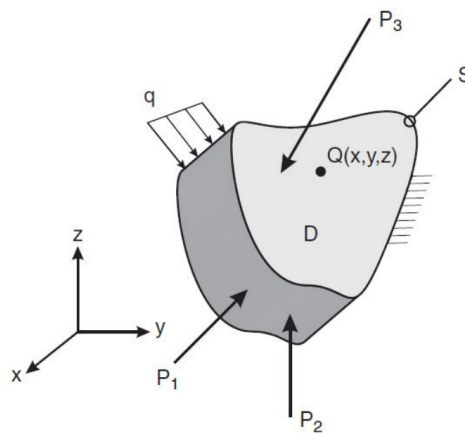
3.1 Reference Systems

A reference system is used to define where a body is located in space. The proper definition of this system becomes necessary as composite laminates are often orthotropic or anisotropic, meaning that their mechanical properties are not the same for every direction and therefore the wrong definition of the reference can cause problems in any structural analysis of composites. Furthermore, VAT panels have curvilinear fiber orientation for each of their plies. This arises the need to have not only a global coordinate to determine the position of the plate in space, but also a second one that defines the orientation of its fibers within the plate itself.

3.1.1 Global Reference System

In a given Cartesian orthogonal system with axes x , y and z , a body in space is considered as a tridimensional mass D of volume V and surface S . It is constrained on a portion of its surface and submitted to concentrated loads P_i , linear loads q , surface loads p , and volumetric loads g as illustrated in Figure 3.1.

Figure 3.1: Representation of a generic 3D body

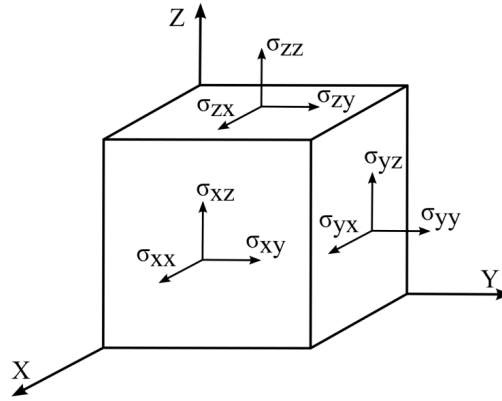


Source: [23]

For any given point in this generic solid, its 3D tension state can be described as a 3x3 tensor \mathbf{T} in 3.1, which components are expressed in terms of σ_{ij} , where i and j represent the direction alongside the stress, and the direction normal to the face in which the stress is applied, respectively. Figure 3.2 shows a graphical representation of this second-order Cauchy stress tensor.

$$\mathbf{T} = \begin{bmatrix} \sigma_{xx} & \sigma_{xy} & \sigma_{xz} \\ \sigma_{yx} & \sigma_{yy} & \sigma_{yz} \\ \sigma_{zx} & \sigma_{zy} & \sigma_{zz} \end{bmatrix} \quad (3.1)$$

Figure 3.2: Graphical representation of Cauchy's second-order stress tensor



Source: [23]

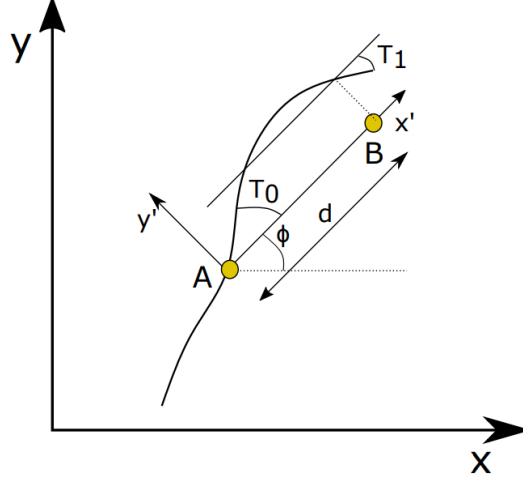
Fortunately, according to Cauchy's Reciprocal Theorem, the tensor can be reduced to only six terms, due to the rotation equilibrium present in this problem.

$$\begin{cases} \sigma_{xy} = \sigma_{yx} = \tau_{xy} \\ \sigma_{xz} = \sigma_{zx} = \tau_{xz} \\ \sigma_{zy} = \sigma_{yz} = \tau_{yz} \end{cases} \quad (3.2)$$

3.1.2 Fiber Reference System

For a given point in the laminate material it is possible to describe a local reference system able to describe the orientation of the fiber $\theta(x')$. To avoid any confusion, the local axes are x' , y' , and z' . Where z' lies alongside the thickness.

Usually, VAT laminae are represented by polynomials or splines. In this work, the curvilinear path for the k-th lamina is defined accordingly to [9] in Equation 3.3, within the fiber reference frame shown in Figure 3.3.

Figure 3.3: Reference system used in a VAT laminate path


Source: [10]

$$\theta^k(x') = \phi^k + T_0^k + (T_1^k - T_0^k) \frac{|x'|}{d} \quad (3.3)$$

Where ϕ^k , T_0^k , T_1^k and d are the inclination angle, the fiber angle at $x = 0$, the fiber angle at $x = d$, and the characteristic distance on the x' axis, respectively. In most scenarios, $\phi = 0^\circ$ or $\phi = 90^\circ$, which means that the reference system of the fibers is either parallel or perpendicular to the global reference system, respectively.

3.2 Geometrical Relations

When addressing displacements, stresses, and strains, the global coordinate system is used. Recalling the simplification done in Equation 3.2, these vectors \mathbf{u} , $\boldsymbol{\sigma}$, and $\boldsymbol{\epsilon}$ can all be written in Equations 3.4, 3.5, and 3.6, respectively.

$$\mathbf{u}^T(x, y, z) = \{u_x \quad u_y \quad u_z\} \quad (3.4)$$

$$\boldsymbol{\sigma}^T = \{\sigma_{xx} \quad \sigma_{yy} \quad \sigma_{zz} \quad \tau_{xz} \quad \tau_{yz} \quad \tau_{xy}\} \quad (3.5)$$

$$\boldsymbol{\epsilon}^T = \{\epsilon_{xx} \quad \epsilon_{yy} \quad \epsilon_{zz} \quad \gamma_{xz} \quad \gamma_{yz} \quad \gamma_{xy}\} \quad (3.6)$$

Where the superscript T denotes transposition. For the purposes of this work, it is possible to consider the Infinitesimal Strain Theory, which assumes that the displacements of the material particles of the body are much smaller than any of

its dimensions. This assumption implies that the geometry of the initial body is unchanged by the deformation inflicted on it, consequently making the equations of continuum mechanics much simpler. Equation 3.7

$$\left\{ \begin{array}{l} \epsilon_{xx} = \frac{\partial u_x}{\partial x} = u_{x,x} \\ \epsilon_{yy} = \frac{\partial u_y}{\partial y} = u_{y,y} \\ \epsilon_{zz} = \frac{\partial u_z}{\partial z} = u_{z,z} \\ \gamma_{xz} = \frac{\partial u_x}{\partial z} + \frac{\partial u_z}{\partial x} = u_{x,z} + u_{z,x} \\ \gamma_{yz} = \frac{\partial u_y}{\partial z} + \frac{\partial u_z}{\partial y} = u_{y,z} + u_{z,y} \\ \gamma_{xy} = \frac{\partial u_x}{\partial y} + \frac{\partial u_y}{\partial x} = u_{x,y} + u_{y,x} \end{array} \right. \quad (3.7)$$

In matrix notation, the previous equation becomes:

$$\boldsymbol{\epsilon} = \mathbf{b}\mathbf{u} \quad (3.8)$$

$$\mathbf{b} = \begin{bmatrix} \frac{\partial}{\partial x} & 0 & 0 \\ 0 & \frac{\partial}{\partial y} & 0 \\ 0 & 0 & \frac{\partial}{\partial z} \\ \frac{\partial}{\partial z} & 0 & \frac{\partial}{\partial x} \\ 0 & \frac{\partial}{\partial z} & \frac{\partial}{\partial y} \\ \frac{\partial}{\partial y} & \frac{\partial}{\partial x} & 0 \end{bmatrix} \quad (3.9)$$

3.3 Equilibrium Equations

To be considered in equilibrium, the aforementioned body of mass M and volume V must satisfy the Equations in 3.10.

$$\left\{ \begin{array}{l} \frac{\partial \sigma_{xx}}{\partial x} + \frac{\partial \tau_{xy}}{\partial y} + \frac{\partial \tau_{xz}}{\partial z} = g_x \\ \frac{\partial \tau_{xy}}{\partial x} + \frac{\partial \sigma_{yy}}{\partial y} + \frac{\partial \tau_{yz}}{\partial z} = g_y \\ \frac{\partial \tau_{xz}}{\partial x} + \frac{\partial \tau_{yz}}{\partial y} + \frac{\partial \sigma_{zz}}{\partial z} = g_z \end{array} \right. \quad (3.10)$$

Where g_x , g_y , and g_z are the unit body forces, such as inertia and weight. In a more compact form they can be written in the form of vectors.

$$\mathbf{b}^T \boldsymbol{\sigma} = \mathbf{g} \quad (3.11)$$

Where \mathbf{b} is the differential operator defined in Equation 3.9 and \mathbf{g} is:

$$\mathbf{g}^T = \{g_x \quad g_y \quad g_z\} \quad (3.12)$$

3.4 Boundary Conditions

When regarding the generic body previously described, it is possible to define two types of boundary conditions, those that constrain its mechanical characteristics and those that constrain the geometrical ones. As these conditions are applied on the surface S of the body, it is convenient to divide it into two regions S_m and S_g , which refer to the mechanical BC and geometrical ones. Therefore, it is possible to define equations for both surfaces. In the case of surface S_m , the mechanical boundaries are:

$$\begin{cases} \sigma_{xx}n_x + \tau_{xy}n_y + \tau_{xz}n_z = p_x \\ \tau_{xy}n_x + \sigma_{yy}n_y + \tau_{yz}n_z = p_y \\ \tau_{xz}n_x + \tau_{yz}n_y + \sigma_{zz}n_z = p_z \end{cases} \quad (3.13)$$

Where $\mathbf{n} = (n_x, n_y, n_z)$ is the normal vector of surface S_m and $\mathbf{p} = (p_x, p_y, p_z)$ is the unit force vector also relative to S_m . In the case of surface S_g the geometrical boundaries are:

$$\begin{cases} u_x = \bar{u}_x \\ u_y = \bar{u}_y \\ u_z = \bar{u}_z \end{cases} \quad (3.14)$$

Where $\bar{u}_x, \bar{u}_y, \bar{u}_z$ are the displacements set at the geometrical boundary. These equations can also be written in compact form as:

$$\mathbf{u} = \bar{\mathbf{u}} \quad (3.15)$$

3.5 Constitutive Equations

In the field of engineering, a constitutive equation is a relation between two physical quantities. For structural analysis is very important to define how mechanical stress connects to strain. From the previous assumptions of small displacements, it is also possible to use Hooke's law to build a linear relationship between these physical quantities.

$$\begin{Bmatrix} \sigma_{xx} \\ \sigma_{yy} \\ \sigma_{zz} \\ \sigma_{xz} \\ \sigma_{yz} \\ \sigma_{xy} \end{Bmatrix} = \begin{bmatrix} C_{11} & C_{12} & C_{13} & 0 & 0 & 0 \\ C_{12} & C_{22} & C_{23} & 0 & 0 & 0 \\ C_{13} & C_{23} & C_{33} & 0 & 0 & 0 \\ 0 & 0 & 0 & C_{44} & 0 & 0 \\ 0 & 0 & 0 & 0 & C_{55} & 0 \\ 0 & 0 & 0 & 0 & 0 & C_{66} \end{bmatrix} \begin{Bmatrix} \epsilon_{xx} \\ \epsilon_{yy} \\ \epsilon_{zz} \\ \gamma_{xz} \\ \gamma_{yz} \\ \gamma_{xy} \end{Bmatrix} \quad (3.16)$$

Where \mathbf{C} is the stiffness matrix for an orthotropic material, which is the case for composites. Hooke's Law can also be written in a more compact form as:

$$\boldsymbol{\sigma} = \mathbf{C}\boldsymbol{\epsilon} \quad (3.17)$$

In some cases it is also important to build the inverse of the stiffness matrix, the flexibility matrix. As both of them are symmetric, they have the same non-zero elements, as one can see on Equation 3.18.

$$\mathbf{C}^{-1} = \mathbf{S} = \begin{bmatrix} S_{11} & S_{12} & S_{13} & 0 & 0 & 0 \\ S_{12} & S_{22} & S_{23} & 0 & 0 & 0 \\ S_{13} & S_{23} & S_{33} & 0 & 0 & 0 \\ 0 & 0 & 0 & S_{44} & 0 & 0 \\ 0 & 0 & 0 & 0 & S_{55} & 0 \\ 0 & 0 & 0 & 0 & 0 & S_{66} \end{bmatrix} \quad (3.18)$$

Furthermore, the flexibility terms of this matrix can be written explicitly in function of moduli of Young E_i , moduli of shear G_{ij} , and Poisson coefficients ν_{ij} . Once again, the inherent symmetry of this matrix makes it possible to have Equation 3.19.

$$\frac{\nu_{ij}}{E_i} = \frac{\nu_{ji}}{E_j} \quad (i, j = 1, 2, 3) \quad (3.19)$$

Which finally results in the explicit flexibility matrix 3.20.

$$\mathbf{S} = \begin{bmatrix} \frac{1}{E_1} & -\frac{\nu_{12}}{E_1} & -\frac{\nu_{13}}{E_1} & 0 & 0 & 0 \\ -\frac{\nu_{12}}{E_1} & \frac{1}{E_2} & -\frac{\nu_{23}}{E_2} & 0 & 0 & 0 \\ -\frac{\nu_{13}}{E_1} & -\frac{\nu_{23}}{E_2} & \frac{1}{E_3} & 0 & 0 & 0 \\ 0 & 0 & 0 & \frac{1}{G_{23}} & 0 & 0 \\ 0 & 0 & 0 & 0 & \frac{1}{G_{13}} & 0 \\ 0 & 0 & 0 & 0 & 0 & \frac{1}{G_{12}} \end{bmatrix} \quad (3.20)$$

Nevertheless, the stiffness matrix in Equation 3.16 is built considering a material reference system. For this work it would be desirable to write it in the global reference system. Hence, according to [37] to convert \mathbf{C} into the global reference system, it is conveniently rotated around the out-of-plane axis of the laminate, the z axis. Equation 3.21 shows the final result.

$$\mathbf{C}_{global} \begin{bmatrix} C_{11} & C_{12} & C_{13} & 0 & 0 & C_{16} \\ C_{12} & C_{22} & C_{23} & 0 & 0 & C_{26} \\ C_{13} & C_{23} & C_{33} & 0 & 0 & C_{36} \\ 0 & 0 & 0 & C_{44} & C_{45} & 0 \\ 0 & 0 & 0 & C_{45} & C_{55} & 0 \\ C_{16} & C_{26} & C_{36} & 0 & 0 & C_{66} \end{bmatrix} \quad (3.21)$$

Where the terms C_{16} , C_{26} , and C_{36} introduce a coupling bending and in-plane loads, which means that these loads can generate a moment of forces. Still, Equation 3.21 is not sufficient to describe the behavior of a VAT laminate. It is necessary to recall that the fibers have a variable orientation defined in its own reference system, which implies that \mathbf{C}_{global} depends on the position where it is being calculated, it depends on the cartesian in-plane coordinates x and y . Hence, the new stiffness matrix $\tilde{\mathbf{C}}(x, y)$ is computed as in Equation 3.22.

$$\tilde{\mathbf{C}}(x, y) = \mathbf{T}(x, y)\mathbf{C}(\mathbf{T}(x, y))^T \quad (3.22)$$

Where $\mathbf{T}(x, y)$ is the rotation matrix that converts \mathbf{C}_{global} from global coordinates to $\tilde{\mathbf{C}}(x, y)$ with fiber coordinates:

$$\mathbf{T}(x, y) = \begin{bmatrix} \cos^2 \theta(x, y) & \sin^2 \theta(x, y) & 0 & 0 & 0 & \sin 2\theta(x, y) \\ \sin^2 \theta(x, y) & \cos^2 \theta(x, y) & 0 & 0 & 0 & -\sin 2\theta(x, y) \\ 0 & 0 & 1 & 0 & 0 & 0 \\ 0 & 0 & 0 & \cos \theta(x, y) & -\sin \theta(x, y) & 0 \\ 0 & 0 & 0 & -\sin \theta(x, y) & \cos \theta(x, y) & 0 \\ \sin \theta(x, y) \cos \theta(x, y) & -\sin \theta(x, y) \cos \theta(x, y) & 0 & 0 & 0 & \cos^2 \theta(x, y) - \sin^2 \theta(x, y) \end{bmatrix} \quad (3.23)$$

And the final form of the Hooke's Law in compact vector form becomes:

$$\boldsymbol{\sigma} = \tilde{\mathbf{C}}(x, y)\boldsymbol{\epsilon} \quad (3.24)$$

3.6 Governing Equations

Until the present section, all the work developed was to define the problem of VAT laminates. In summary, there are a total of 15 unknowns, 6 stress components, 6 strain components and 3 displacement components, for 15 equations, the equilibrium, the boundary conditions, the geometrical relations and Hooke's Law. A common way to approach the solution of all these equations is by making substitutions to express them solely in terms of the displacements \mathbf{u} .

3.6.1 Principle of Virtual Displacements: Strong Form

To begin the solution of this problem the Principle of Virtual Work (PVW) is used. The PVW enounces that if a mechanical system is in equilibrium considering all the loads and all of its constraints, then the sum of all the virtual work of the forces applied to it are zero. In the specific case that the elastic problem is written in terms of the displacements, the PVW is called Principle of the Virtual Displacements (PVD). In this work, only static cases shall be contemplated, meaning that body forces such as inertia should be disconsidered, resulting in Equation 3.25.

$$\delta L_{int} = \delta L_{ext} \quad (3.25)$$

Where δL_{int} and δL_{ext} represent the internal elastic work done by external forces, respectively. The δ is used to indicate an infinitesimal variation, or rather, a virtual variation of the physical quantity. Developing even further, the internal work can be expressed as sum of all the stress components multiplied by their corresponding virtual strain and integrated over the mechanical body of volume V .

$$\delta L_{int} = \int_V (\sigma_{xx} \delta \epsilon_{xx} + \sigma_{yy} \delta \epsilon_{yy} + \sigma_{zz} \delta \epsilon_{zz} + \tau_{xz} \delta \gamma_{xz} + \tau_{yz} \delta \gamma_{yz} + \tau_{xy} \delta \gamma_{xy}) dV \quad (3.26)$$

Which in compact vector form becomes:

$$\delta L_{int} = \int_V \delta \boldsymbol{\epsilon}^T \boldsymbol{\sigma} dV \quad (3.27)$$

Substituting Equation 3.7 into Equation 3.27 it is possible to obtain the internal work in terms of the displacements vector \mathbf{u} .

$$\delta L_{int} = \int_V \delta (\mathbf{b}\mathbf{u})^T \boldsymbol{\sigma} dV = \int_V \delta (\mathbf{u}^T \mathbf{b}^T) \boldsymbol{\sigma} dV \quad (3.28)$$

Next, it is necessary to obtain the integral form of elastic problem, also know as the strong form. So, integrating the right hand side of Equation 3.28 by parts.

$$\int_V \delta (\mathbf{u}^T \mathbf{b}^T) \boldsymbol{\sigma} dV = - \int_V \delta \mathbf{u}^T (\mathbf{b}^T \boldsymbol{\sigma}) dV + \int_S \delta \mathbf{u}^T (\mathbf{I}_n^T \boldsymbol{\sigma}) dS \quad (3.29)$$

Where \mathbf{I}_n is the direction cosine matrix that transforms $\boldsymbol{\sigma}$ into a reference frame normal to the surface S at a generic point P. It can be explicitly written as:

$$\mathbf{I}_n = \begin{bmatrix} n_x & 0 & 0 \\ 0 & n_y & 0 \\ 0 & 0 & n_z \\ n_z & 0 & n_x \\ 0 & n_z & n_x \\ n_y & n_x & 0 \end{bmatrix} \quad (3.30)$$

As the internal work has been fully developed and expressed in terms of \mathbf{u} , it is now necessary to develop a similar procedure for the external work δL_{ext} . It is defined as the sum of the volume forces \mathbf{g} , the surface forces \mathbf{p} , the linear loads \mathbf{q} and the punctual loads \mathbf{P} , which all respectively act over the generic geometries volume V , surface S , line L , and point Q of the mechanical body in question. Hence, it is possible to write:

$$\delta L_{ext} = \int_V \delta \mathbf{u}^T \mathbf{g} dV + \int_S \delta \mathbf{u}^T \mathbf{p} dS + \int_L \delta \mathbf{u}^T \mathbf{q} dy + \delta \mathbf{u}_Q^T \mathbf{P} \quad (3.31)$$

Inserting the definitions of the internal work in Equations 3.28 and 3.29, and the definition of external work in Equation 3.31 into the initial definition of the PVD in Equation 3.31, the following is obtained:

$$\begin{aligned} & - \int_V \delta \mathbf{u}^T (\mathbf{b}^T \boldsymbol{\sigma}) dV + \int_S \delta \mathbf{u}^T (\mathbf{I}_n^T \boldsymbol{\sigma}) dS = \\ & = \int_V \delta \mathbf{u}^T \mathbf{g} dV + \int_S \delta \mathbf{u}^T \mathbf{p} dS + \int_L \delta \mathbf{u}^T \mathbf{q} dy + \delta \mathbf{u}_Q^T \mathbf{P} \end{aligned} \quad (3.32)$$

Nevertheless, Equation 3.32 needs to be adjusted in such a way that all the integrals are over the same domain. To achieve this, the equilibrium equation is recalled. For a generic point P internal to the generic volume V :

$$\mathbf{b}^T \boldsymbol{\sigma} = \mathbf{g} \quad (3.33)$$

Considering next the surface integral, the boundary conditions provide:

$$\mathbf{I}_n^T \boldsymbol{\sigma} = \mathbf{p} \quad (3.34)$$

Combining Equations 3.33, 3.34, and Hooke's Law from Equation 3.17, it is possible to write the differential matrix \mathbf{b} , the unit body forces vector \mathbf{g} , and the stiffness matrix in fiber coordinates in terms of the unknown displacements \mathbf{u} .

$$-\mathbf{b}^T \tilde{\mathbf{C}} \mathbf{b} \mathbf{u} = \mathbf{g} \quad (3.35)$$

Which can be conveniently written as a linear system of equations:

$$\mathbf{k} \mathbf{u} = \mathbf{g} \quad (3.36)$$

Where the new 3x3 matrix \mathbf{k} is:

$$\mathbf{k} = -\mathbf{b}^T \tilde{\mathbf{C}} \mathbf{b} \quad (3.37)$$

$$\mathbf{k} = \begin{bmatrix} k_{xx} & k_{xy} & k_{xz} \\ k_{yx} & k_{yy} & k_{yz} \\ k_{zx} & k_{zy} & k_{zz} \end{bmatrix} \quad (3.38)$$

This means that if the coefficients of matrix $\tilde{\mathbf{C}}$ are known, the linear system is "strong", meaning its solution may be calculated in every point of the domain, or rather, in every point of the body of mass M and volume V . But this poses the disadvantage of only being valid when the body is continuous, which is not the case for most real applications. Hence, an approximate solution known as the "weak" form is developed.

3.6.2 Principle of Virtual Displacements: Weak Form

The weak form of the PVD can be obtained by approximating the generic body into points connected by lines, or rather, nodes and edges. So the body instead of being continuous, is discretely composed by a finite number of shapes built by these so called nodes and edges. The first consequence of this discretization becomes evident when defining the new vector of displacements, which can be rewritten as:

$$\mathbf{u} = \mathbf{N}\mathbf{U} \quad (3.39)$$

Where \mathbf{N} is the matrix of shape functions and \mathbf{U} is the vector of nodal displacements. This means that the displacement of the whole body can be approximated by the displacement multiplied by a function that describes how one node is connected to another. If the shape functions are chosen wisely, then by increasing the amount of nodes representing the body, the displacements will tend towards the exact ones. With Equation 3.39, it is possible to derive the definition of the virtual external work.

$$\delta L_{ext} = \delta \mathbf{U}^T \mathbf{P} \quad (3.40)$$

Where \mathbf{P} is the vector of nodal forces.

$$\mathbf{P}^T = \{P_{x1} \ P_{y1} \ P_{z1} \ P_{x1} \ P_{y1} \ P_{z1} \ \dots \ P_{xNE} \ P_{yNE} \ P_{zNE}\} \quad (3.41)$$

And \mathbf{U} is similarly written as:

$$\mathbf{U}^T = \{u_{x1} \ u_{y1} \ u_{z1} \ u_{x1} \ u_{y1} \ u_{z1} \ \dots \ u_{xNE} \ u_{yNE} \ u_{zNE}\} \quad (3.42)$$

Both vectors have a total of $3 \times N_{NE}$ components (3 times the total amount of nodes). Furthermore, Equations 3.8 and 3.17 can be brought back with:

$$\boldsymbol{\epsilon} = \mathbf{b}\mathbf{u} = \mathbf{b}\mathbf{N}\mathbf{U} = \mathbf{B}\mathbf{U} \quad (3.43)$$

$$\boldsymbol{\sigma}' = \mathbf{C}\boldsymbol{\epsilon} = \mathbf{C}\mathbf{B}\mathbf{U} \quad (3.44)$$

Where matrix \mathbf{B} is readily obtained by applying the differential vector \mathbf{b} to the shape function matrix \mathbf{N} . It is also possible to apply the concept of virtual variations to Equation 3.39, resulting in:

$$\delta\mathbf{u} = \mathbf{N}\delta\mathbf{U} \quad (3.45)$$

And defining the internal virtual work with these new discrete equations:

$$\delta L_{int} = \delta\mathbf{U}^T \left(\int_V \mathbf{B}^T \mathbf{C} \mathbf{B} dV \right) \mathbf{U} = \delta\mathbf{U}^T \mathbf{K} \mathbf{U} \quad (3.46)$$

Where the stiffness matrix \mathbf{K} is:

$$\mathbf{K} = \int_V \mathbf{B}^T \mathbf{C} \mathbf{B} dV \quad (3.47)$$

Once again with the principle of PVD from Equation 3.25, which equalizes the internal and external works from 3.46 and 3.40, respectively:

$$\delta\mathbf{U}^T \mathbf{K} \mathbf{U} = \delta\mathbf{U}^T \mathbf{P} \quad (3.48)$$

Which can be conveniently simplified into the linear system:

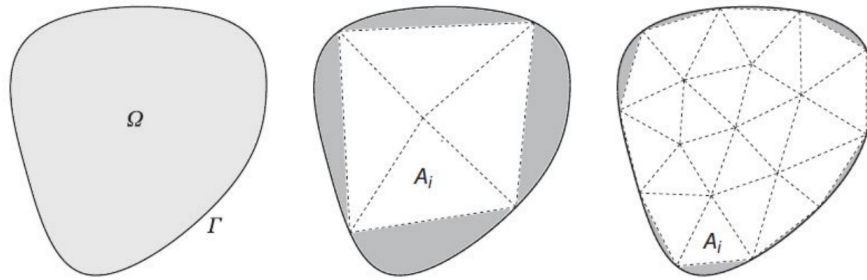
$$\mathbf{K} \mathbf{U} = \mathbf{P} \quad (3.49)$$

Which represents the weak form of the equilibrium equation for a discrete solid body.

3.7 Introduction to FEM

To simulate complex problems involving VAT plates, numerical methods such as the Finite Element Method (FEM) become a necessity. Currently, it is the main instrument used to approach structural analysis because it can be readily implemented into the software. According to [38] the FEM is based on the subdivision of the structure of interest in a finite number of simplified subdomains known as elements, which are attached to each other through nodes. The main idea of this discretization method is to solve the problem in every node of the domain. In the field of structural mechanics, the displacement field is coupled to the nodal displacements through the shape function, which is usually an algebraic polynomial. Figure 3.4 shows a plane domain that has been discretized into triangular elements.

Figure 3.4: Plane domain discretized into triangular elements



Source: [23]

As any other discrete method, the discretization of the domain done in the FEM causes two main types of approximation errors:

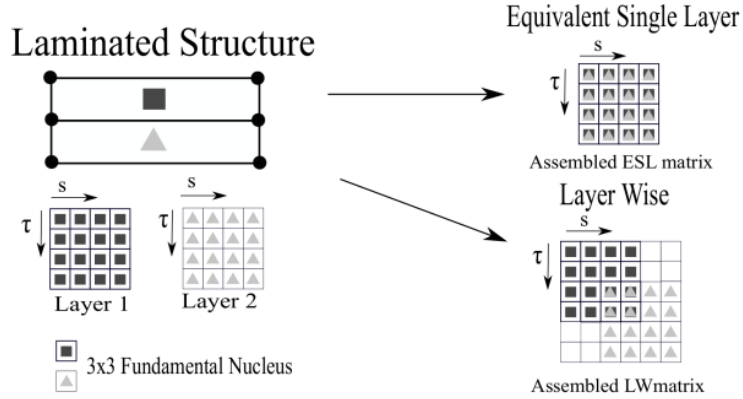
1. **Discretization.** It is the error due to the finite subdivision of the domain, which results in parts of it not being properly represented. As it can be seen in Figure 3.4, not every single point of the plane domain is contemplated by the triangular elements. But, intuitively, by using smaller and smaller elements it is possible to obtain a mesh so fine that it represents the domain with enough precision.
2. **Approximation.** It is due to the simplifications introduced by the shape function. As each of them merely attempts to approximate the interaction between two nodes there comes an error associated to its order. This error can hence be reduced by increasing the order of the functions used.

3.8 Equivalent Single Layer and Layerwise Methods

Before all the formulation for the Finite Element (FE) problem is presented it is worth mentioning that in the literature there are 2 main approaches used to analyze laminated structures, Equivalent Single Layer (ESL) and Layerwise (LW). The first uses a technique that merges all the layers of the composite together, adding their contributions when building the stiffness matrix. In this way, the properties of every lamina are viewed as one. The clear disadvantage of this method is that it is incapable of accurately representing the effects of the individual layers at their interfaces. Contrary to this method, LW considers the effects of each layer separately and guarantees the displacement coupling at their interfaces when forming the stiffness matrix. Obviously, this method requires more computational

effort as the resulting matrix is bigger. Figure 3.5 shows a sketch of the assembly procedure of the stiffness matrix of the two methods.

Figure 3.5: Comparison between the stiffness matrices of ESL and LW methods



Source: [10]

This work instead proposes a different approach. It takes advantage of the simplicity of the ESL theory to calculate global results and builds a refined 3D local model to more carefully evaluate regions of interest, namely free-edges, or any other low-safety-margin parts of the component.

3.9 Global Model FEM

In this work, the global model is built according to two theories, the Equivalent Single Layer (ESL) and the Classical Laminate Plate (CLPT). The first simplifies the problem by reducing a heterogeneous laminate composite into a statically equivalent single-layer one, making the problem 2D. The second is an extension of the Kirchhoff-Love plate theory used for thin-layer shells, which neglects the influence of transverse shear stresses and deformations. The two of them combined make computational analyses much more lightweight.

3.9.1 Governing Equations for Thin Plates under Bending

On the previous sections, the governing equations were presented in a general form, able to describe the behavior of a generic VAT laminate. In this subsection, the problem is specifically described for thin VAT plates, which is the case for the global model. CLPT and ESL imply that at any given point of a thin plate the x

and y displacements can be written as:

$$u_x = -z \frac{\partial u_z}{\partial x} \quad (3.50)$$

$$u_y = -z \frac{\partial u_z}{\partial y} \quad (3.51)$$

Where u_z is also known as the plate deflection. The curvatures are given as the rate of change of angular displacements:

$$\kappa_x = -\frac{\partial^2 u_z}{\partial x^2} \quad (3.52)$$

$$\kappa_y = -\frac{\partial^2 u_z}{\partial y^2} \quad (3.53)$$

$$\kappa_{xy} = -2 \frac{\partial^2 u_z}{\partial x \partial y} \quad (3.54)$$

In this theory it is particularly convenient to write the strain definitions in terms of u_z :

$$\epsilon_x = \frac{\partial u_x}{\partial x} = -z \frac{\partial^2 u_z}{\partial x^2} \quad (3.55)$$

$$\epsilon_y = \frac{\partial u_y}{\partial y} = -z \frac{\partial^2 u_z}{\partial y^2} \quad (3.56)$$

$$\gamma_{xy} = \frac{\partial u_x}{\partial x} + \frac{\partial u_y}{\partial y} = -2z \frac{\partial^2 u_z}{\partial x \partial y} \quad (3.57)$$

Recalling the stress-strain relationship from the previous section it can be written that:

$$\begin{Bmatrix} \sigma_x \\ \sigma_y \\ \tau_{xy} \end{Bmatrix} = \begin{bmatrix} \tilde{C}_{11} & \tilde{C}_{12} & \tilde{C}_{16} \\ \tilde{C}_{12} & \tilde{C}_{22} & \tilde{C}_{26} \\ \tilde{C}_{16} & \tilde{C}_{26} & \tilde{C}_{66} \end{bmatrix} \begin{Bmatrix} \epsilon_x \\ \epsilon_y \\ \tau_{xy} \end{Bmatrix} \quad (3.58)$$

Where \tilde{C}_{ij} is the previously defined material matrix. Next, the bending moments are presented as:

$$M_x = \int_{-t/2}^{t/2} z \sigma_x dz \quad (3.59)$$

$$M_y = \int_{-t/2}^{t/2} z \sigma_y dz \quad (3.60)$$

$$M_{xy} = \int_{-t/2}^{t/2} z \tau_{xy} dz \quad (3.61)$$

Where t is the thickness of the plate. The governing equations may then be written as:

$$\begin{cases} \frac{\partial Q_x}{\partial x} + \frac{\partial Q_y}{\partial y} + q = 0 \\ \frac{\partial M_x}{\partial x} + \frac{\partial M_{xy}}{\partial y} - Q_x = 0 \\ \frac{\partial M_{xy}}{\partial x} + \frac{\partial M_y}{\partial y} - Q_y = 0 \end{cases} \quad (3.62)$$

Where q is a transverse distributed load and Q_x and Q_y are transverse shear line loads. Using all of the previous equation, it is possible to write all of the governing ones in terms of the out-of-plane displacement u_z .

3.9.2 FEM for Thin Plates under Bending

The most common type of element for this case is the rectangular, 12-degree-of-freedom one. As the name suggests, it is a 2D rectangle with 4 nodes, each having 3 DoF, the vertical displacement and the rotations on x and y .

$$\mathbf{u}^T = \{u_{zi} \quad \theta_{xi} \quad \theta_{yi}\} \quad (3.63)$$

Where the rotations are defined as:

$$\theta_x = \frac{\partial u_z}{\partial y} \quad (3.64)$$

$$\theta_y = -\frac{\partial u_z}{\partial x} \quad (3.65)$$

As the plate element under development had 12-dof, a corresponding 12-term polynomial needs to be selected as the displacement function that approximates the u_z in function of x and y :

$$\begin{aligned} u_z(x, y) = a_1 + a_2x + a_3y + a_4x^2 + a_5xy + a_6y^2 + a_7x^3 + a_8x^2y + \\ + a_9xy^2 + a_{10}y^3 + a_{11}x^3y + a_{12}xy^3 \end{aligned} \quad (3.66)$$

Where the constants a_j are determined through specific boundary conditions of each problem. The previous equation can also be expressed in matrix form as:

$$\begin{Bmatrix} u_z \\ \frac{\partial u_z}{\partial y} \\ -\frac{\partial u_z}{\partial x} \end{Bmatrix} = \begin{bmatrix} 1 & x & y & x^2 & xy & y^2 & x^3 & x^2y & xy^2 & y^3 & x^3y & xy^3 \\ 0 & 0 & 1 & 0 & x & 2y & 0 & x^2 & 2xy & 3y^2 & x^3 & 3xy^2 \\ 0 & -1 & 0 & -2x & -y & 0 & -3x^2 & -2xy & -y^2 & 0 & -3x^2y & -y^3 \end{bmatrix} \begin{Bmatrix} a_1 \\ a_2 \\ a_3 \\ \vdots \\ a_{12} \end{Bmatrix} \quad (3.67)$$

Or rather in compact form:

$$\boldsymbol{\psi} = \mathbf{P}\mathbf{a} \quad (3.68)$$

Once the boundary conditions have been applied, and the constants \mathbf{a} found, it is possible to calculate the displacements \mathbf{U} for every node with:

$$\begin{Bmatrix} u_{z1} \\ \theta_{x1} \\ \theta_{y1} \\ \vdots \\ u_{zN} \\ \theta_{xN} \\ \theta_{yN} \end{Bmatrix} = \begin{bmatrix} 1 & x_1 & y_1 & x_1^2 & x_1y_1 & y_1^2 & x_1^3 & x_1^2y_1 & x_1y_1^2 & y_1^3 & x_1^3y_1 & x_1y_1^3 \\ \vdots & & & & & & & & & & & \\ 0 & -1 & 0 & -2x_N & -y_N & 0 & -3x_N^2 & -2x_Ny_N & -y_N^2 & 0 & -3x_N^2y_N & -y_N^3 \end{bmatrix} \begin{Bmatrix} a_1 \\ a_2 \\ a_3 \\ \vdots \\ a_{12} \end{Bmatrix} \quad (3.69)$$

Which can be more easily written as:

$$\mathbf{a} = \mathbf{D}_f^{-1}\mathbf{U} \quad (3.70)$$

Substituting Equation 3.70 into Equation 3.68:

$$\boldsymbol{\psi} = \mathbf{P}\mathbf{D}_f^{-1}\mathbf{U} \quad (3.71)$$

$$\boldsymbol{\psi} = \mathbf{N}\mathbf{U} \quad (3.72)$$

Where $\mathbf{N} = \mathbf{P}\mathbf{D}_f^{-1}$ is the shape function matrix. The last step is building the stiffness matrix of the problem. This is achieved by defining the curvature matrix \mathbf{Q} :

$$\begin{Bmatrix} \kappa_x \\ \kappa_y \\ \kappa_{xy} \end{Bmatrix} = \begin{bmatrix} 0 & 0 & 0 & -2 & 0 & 0 & -6x & -2y & 0 & 0 & -6xy & 0 \\ 0 & 0 & 0 & 0 & 0 & -2 & 0 & 0 & -2x & -6y & 0 & -6xy \\ 0 & 0 & 0 & 0 & -2 & 0 & 0 & -4x & -4y & 0 & -6x^2 & -6y^2 \end{bmatrix} \begin{Bmatrix} a_1 \\ a_2 \\ a_3 \\ \vdots \\ a_{12} \end{Bmatrix} \quad (3.73)$$

From the definition of \mathbf{a} in Equation 3.70 it is derived:

$$\boldsymbol{\kappa} = \mathbf{Q}\mathbf{D}_f^{-1}\mathbf{U} \quad (3.74)$$

$$\boldsymbol{\kappa} = \mathbf{B}\mathbf{U} \quad (3.75)$$

Where:

$$\mathbf{B} = \mathbf{Q}\mathbf{D}_f^{-1} \quad (3.76)$$

Furthermore, from the moment-curvature relation comes:

$$\begin{Bmatrix} M_x \\ M_y \\ M_{xy} \end{Bmatrix} = \mathbf{D}\mathbf{B}\mathbf{U} \quad (3.77)$$

Where \mathbf{D} is an orthotropic material matrix. Then finally the stiffness matrix can be found with:

$$\mathbf{K} = \int_S \mathbf{B}^T \mathbf{D} \mathbf{B} dS \quad (3.78)$$

As discussed in the previous development of the PVD, it can be written that:

$$\mathbf{K} \mathbf{U} = \mathbf{F} \quad (3.79)$$

$$\mathbf{F}^T = \{f_{wi} \quad f_{\theta xi} \quad f_{\theta yi}\} \quad (3.80)$$

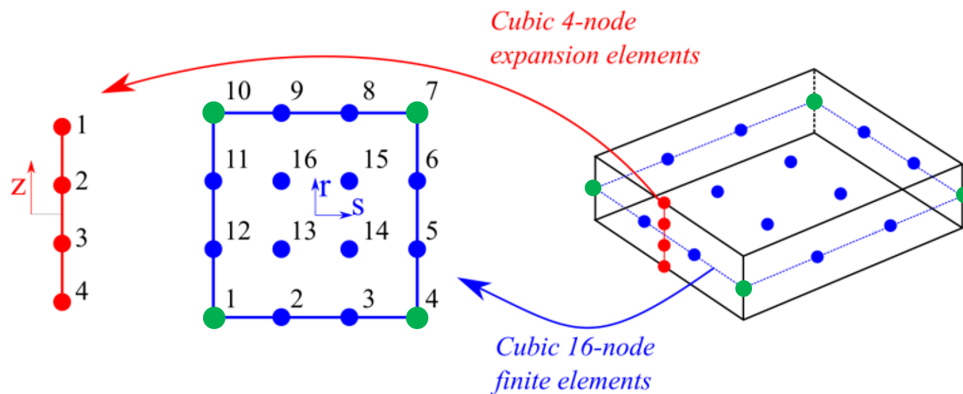
Where \mathbf{F} is the vector of the nodal force and the x and y moments.

3.10 Local Model FEM

The formulation for the local model differs from the global one. It is much more sophisticated as it takes the displacements computed in the global model and uses them as inputs to calculate interlaminar stresses and strains. For this reason, ESL and CLPT can no longer be used. Hence the Carrera Unified Formulation is adopted as the foundation for the local element.

The local CUF element built using cubic interpolations (also called LD3), which means that, for a single layer, it has 16 in-plane nodes and 4 out-of-plane ones, reaching a total of 64. Figure 3.6 brings a graphical representation of this element, where the blue nodes are the local in-plane ones, the red are thickness ones, and the green ones are the ones from the global mesh (nodes 1, 4, 7, and 10). The details of the LD3 interpolations are explicitly described in Appendix A, according to the natural reference system $r - s - z$. It is important to notice that only one

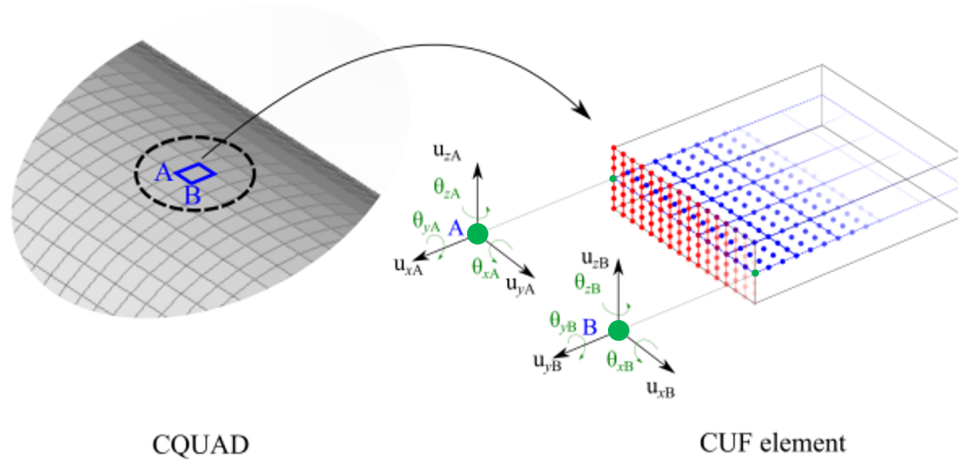
Figure 3.6: Graphical Representation of the local CUF element



Source: [23]

layer of in-plane elements are drawn to keep this sketch less polluted. In reality there would be four layers of blue nodes. The coupling between the global and the local models is done by retrieving the displacements and rotations from the global nodes and using them as inputs to the cubic interpolation that builds the local CUF element. Figure 3.7 shows how a 2D CQUAD square laminate plate element with 2 layers is transformed into a $5 \times 5 \times 2$ local mesh. Once again, the green dots A and B represent the nodes coming from the global mesh.

Figure 3.7: Graphical Representation of the local CUF element



Source: [23]

3.10.1 Carrera Unified Formulation

The Carrera Unified Formulation (CUF) is a multi-model technique that allows the assembly of the stiffness matrices of single elements through the use of the fundamental nuclei ([39]). This method has an advantage in comparison to others, because of its compatibility with a large class of models, such as an equivalent single layer, layer-wise, and mixed formulation in a unified manner, which makes it effective in a number of different analyses. According to the CUF, it is possible to express the equation of the displacement field $\mathbf{u}(x, y, z)$ and express it as an expansion of the primary unknowns, ([40]):

$$\mathbf{u}(x, y, z) = F_\tau(z)\mathbf{u}_\tau(x, y), \quad \tau = 1, 2, \dots, M \quad (3.81)$$

Where \mathbf{u}_τ , M and $F_\tau(z)$ are the vectors of general displacements, the number of the expansion terms, and the arbitrary cross-section depending on x and z . In this work, the $F_\tau(z)$ adopts the format of the Lagrange Expansions for CUF-based

models. For high-order models, the formulation of the N-th expansion takes the form of:

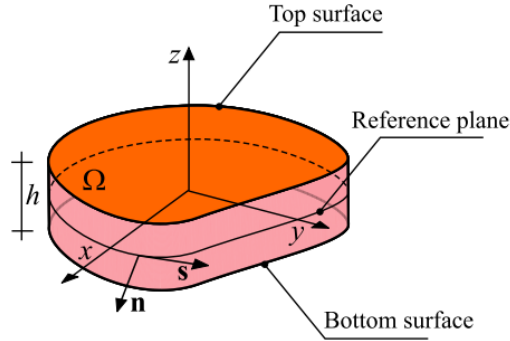
$$\mathbf{u} = F_1\mathbf{u}_1 + F_2\mathbf{u}_2 + F_3\mathbf{u}_3 + \dots + F_N\mathbf{u}_N \quad (3.82)$$

Where:

$$\begin{cases} F_\tau = \frac{1}{4}(r^2 + rr_\tau)(s^2 + ss_\tau) & \text{if } \tau = 1,3,5,7,\dots \\ F_\tau = \frac{1}{2}s_\tau^2(s^2 - ss_\tau) + \frac{1}{2}r_\tau^2(r^2 - rr_\tau)(1 - s^2) & \text{if } \tau = 2,4,6,8,\dots \\ F_\tau = (1 - r^2)(1 - s^2) & \text{if } \tau = N \end{cases} \quad (3.83)$$

Where r and s range from -1 to +1 and r_τ and s_τ are the locations of the roots. In this particular case, it is useful to write the displacements in terms of the top and bottom surfaces as $\mathbf{u}_t = \mathbf{u}_1$ and $\mathbf{u}_b = \mathbf{u}_N$. Figure 3.8 shows the notations used for referencing the top and bottom surfaces of a generic plate of thickness h , with respect to the reference plane.

Figure 3.8: Notation used to define the top and bottom surfaces of a plate



Source: [41]

The introduction of this top and bottom notation into Equation 3.81 results in:

$$\mathbf{u} = F_t\mathbf{u}_t + F_\tau\mathbf{u}_\tau + F_b\mathbf{u}_b \quad \tau = 2,3,\dots,N-1 \quad (3.84)$$

Where:

$$F_t = F_1; \quad F_\tau = F_\tau; \quad F_b = F_N; \quad \mathbf{u}_t = \mathbf{u}_1; \quad \mathbf{u}_b = \mathbf{u}_N \quad (3.85)$$

3.10.2 Local FEM with CUF

It is now possible to bring the concepts developed by the PVD along the new definition for the displacements from CUF, in order to obtain the FEM using CUF. So, as usual, the generalized displacements are defined as functions of the nodal vectors and their corresponding shape functions:

$$\mathbf{u}_\tau(x, y) = N_i(x, y)\mathbf{u}_{\tau i} ; \quad i = 1, 2, \dots, N_{elem} \quad (3.86)$$

To obtain the general displacements in light of the previous discretization, Equation 3.86 is substituted back into Equation 3.81:

$$\mathbf{u}(x, y, z) = F_\tau(z)N_i(x, y)\mathbf{u}_{\tau i} ; \quad \tau = 1, 2, \dots, M ; \quad i = 1, 2, \dots, N_{elem} \quad (3.87)$$

Once again, the concept the PVD can be used to write the virtual displacements as:

$$\delta\mathbf{u} = F_\tau(z)N_i(x, y)\delta\mathbf{u}_{\tau i} \quad (3.88)$$

By substituting the geometrical relations previously developed, it is possible to write the strain and stress vectors:

$$\boldsymbol{\epsilon}(x, y, z) = \mathbf{b}N_i(x, y)F_\tau(z)\mathbf{u}_{\tau i} \quad (3.89)$$

$$\delta\boldsymbol{\epsilon}(x, y, z) = \mathbf{b}N_j(x, y)F_s(z)\mathbf{u}_{s i} \quad (3.90)$$

$$\boldsymbol{\sigma}(x, y, z) = \mathbf{C}N_i(x, y)F_\tau(z)\mathbf{u}_{\tau i} \quad (3.91)$$

The stiffness matrix \mathbf{K}_T is then found by substituting the CUF and FEM approximations defined in Equation 3.87 and the constitutive law of VAT laminates in Equation 3.3 into Equation 3.92:

$$\delta(L_{int}) = \int_V \delta(\delta\boldsymbol{\epsilon}^T \boldsymbol{\sigma}) dV = \delta\mathbf{q}_{s j}^T \mathbf{K}^{i j \tau s} \mathbf{q}_{\tau i} \quad (3.92)$$

Where V is the volume of the local model and $\mathbf{K}^{i j \tau s}$ is the stiffness matrix in the form of a 3×3 fundamental nucleus. For clarity purposes, the terms $\mathbf{k}_{xx}^{i j \tau s}$ and $\mathbf{k}_{xy}^{i j \tau s}$ are described as:

$$\begin{aligned}
 k_{xx}^{\hat{i}j\tau s} &= C_{11} \int_t F_\tau F_s dz \int_\Omega N_{i,x} N_{j,x} d\Omega + C_{44} \int_t F_{\tau,z} F_{s,z} dz \int_\Omega N_i N_j d\Omega + \\
 &+ C_{66} \int_t F_\tau F_s dz \int_\Omega N_{i,y} N_{j,y} d\Omega + C_{16} \int_t F_\tau F_s dz \int_\Omega N_{i,x} N_{j,y} d\Omega + \quad (3.93) \\
 &+ C_{16} \int_t F_\tau F_s dz \int_\Omega N_{i,y} N_{j,x} d\Omega
 \end{aligned}$$

$$\begin{aligned}
 k_{yy}^{\hat{i}j\tau s} &= C_{12} \int_t F_\tau F_s dz \int_\Omega N_{i,y} N_{j,x} d\Omega + C_{66} \int_t F_{\tau,z} F_{s,z} dz \int_\Omega N_{i,x} N_{j,y} d\Omega + \\
 &+ C_{45} \int_t F_{\tau,z} F_{s,z} dz \int_\Omega N_i N_j d\Omega + C_{26} \int_t F_\tau F_s dz \int_\Omega N_{i,y} N_{j,y} d\Omega + \quad (3.94) \\
 &+ C_{16} \int_t F_\tau F_s dz \int_\Omega N_{i,x} N_{j,x} d\Omega
 \end{aligned}$$

Chapter 4

Global-Local Approach

The groundwork that supports all the analyses performed has now been explained and it is now possible to begin the real implementation of the theories presented.

This chapter shall present how the global model is built using software and its results exported so that the local model finishes the interlaminar stress-strain analyses. This process is presented in the form of a workflow for simulating VAT laminates in FEMAP. The assembly of the global model is presented in two different ways:

1. **The splines method.** It explains the current form through which a user can use Femap to make analyses using Femap and the MUL@GL plug-in;
2. **The API.** It shows the development of an Application Program Interface script (API) that overcomes the limitations of the Splines Method and enables the simulation of VAT laminates.

Conversely, the local model is formulated exclusively via one method, which is applied by the MUL2@GL plug-in.

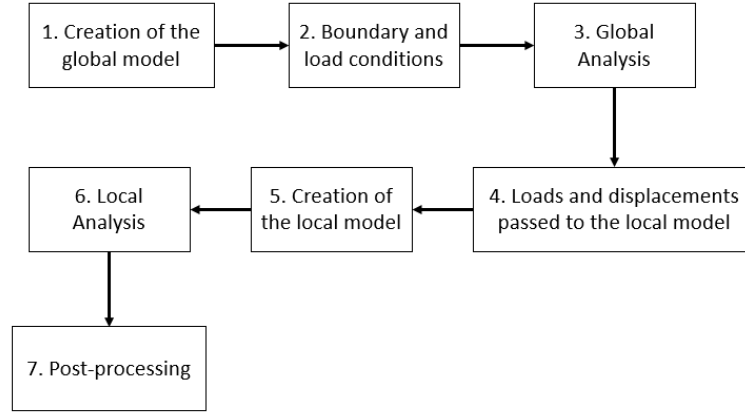
4.1 Global-Local Methodology

The global-local strategy proposed in this paper roughly consists in two steps:

1. **Global Analysis.** The global model is built within the FEMAP Graphic User Interface (GUI) considering NASTRAN's laminated plate elements, then it is solved for given boundary and loading conditions.
2. **Local Analysis.** The global results are collected and a plug-in known as MUL2@GL developed by the MUL2 lab from Politecnico di Torino runs the local analysis for the desired elements.

This two-step workflow can be broken down into a diagram, Figure ??:

Figure 4.1: Global-Local methodology diagram



Source: The author

4.2 The splines method

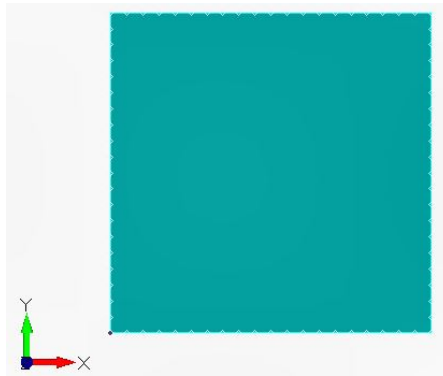
The current way in which it is possible to generate the Global model of a VAT laminate in FEMAP is by creating splines on top of your desired surface and having the material orientation of its elements follow them. FEMAP cannot natively receive variable angle fiber inputs for each individual layer of a laminate. For example, if a user wants to create a simple model of a 1-meter length square plate with only one layer oriented accordingly to Equation 4.1.

$$\theta_{(x,y)}^1 = -45|x| + 90^\circ \quad (4.1)$$

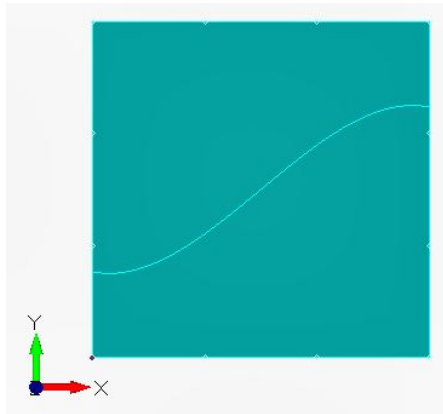
The geometry is then created in FEMAP's graphic environment. As in Figure 4.2. As Equation 4.1 cannot be directly input into FEMAP, it needs to be first transformed into a parametric spline through the method of the Least Squares. The equation that best approximates the desired orientation is found through the Least Squares Method for a third degree polynomial and is represented in Equation 4.2.

$$\theta_{(x,y,z)}^1 \approx -1.44x^3 + 0.842x \quad (4.2)$$

Having the spline equation, it can be loaded into FEMAP, and then the mesh is created with two-dimensional square elements that have their material orientation set accordingly to the approximated spline. Figure 4.3 shows the spline created in the same plane as the plate and Figure 4.4 shows the meshed surface with square elements and their material orientation is shown in the form arrows.

Figure 4.2: Square plate with 1-meter side

Source: The author

Figure 4.3: Spline definition for the fiber orientation

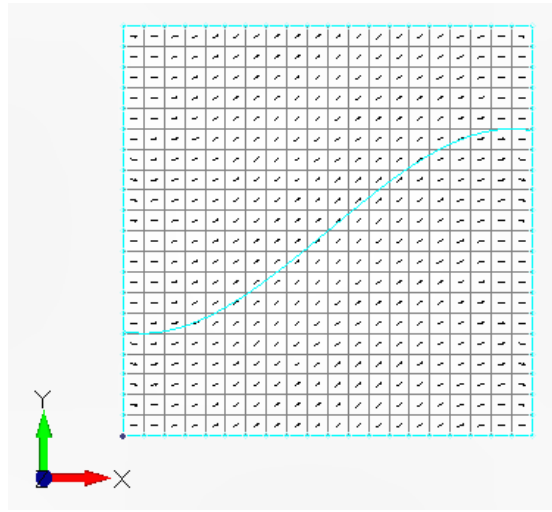
Source: The author

4.2.1 Limitations

This method is limited in two ways, the approximation of the splines introduces an additional error to the calculations; and with FEMAP's interface alone, a user cannot define an individual material orientation for each layer of a laminate.

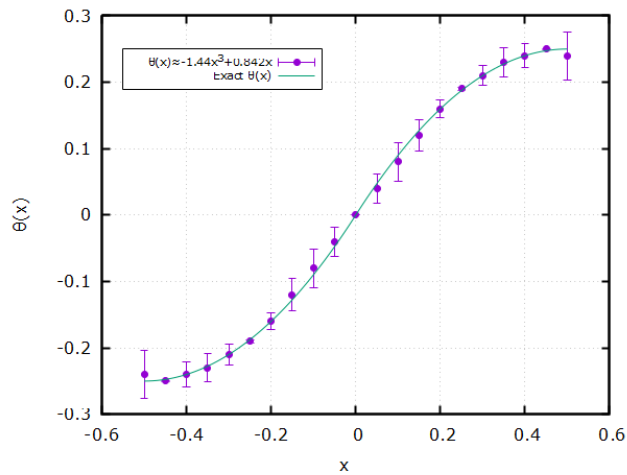
By plotting both the exact angular function in Equation 4.1 and its approximation in Equation 4.2 it is possible to see in Figure 4.5 that despite being visually similar, the functions produce a very significant error. The error represented in bars is multiplied by a factor of 8, to improve its visualization. The most significant one is at the boundary of the function, where it can reach up to 4%. While this is not an unacceptable error for the calculation of displacements, this might propagate and generate larger errors in the calculation of stresses. It is worth mentioning that this error might be even higher for other functions.

Figure 4.4: Square plate with 1-meter side



Source: The author

Figure 4.5: Approximation error of the splines



Source: The author

Furthermore, as FEMAP uses NASTRAN as its solver, it is limited to the PCOMP property card, which is used to define the property of laminate plate elements. This card defines within itself; the material; the thickness; the fiber angle; and the failure theory for each ply of the element. In particular, the fiber orientation is set for each ply as a constant rotation from the material orientation of the element, which means that each layer cannot have an individual angle function.

Hence, this issue can only be solved by creating an individual property card for

each element of the structure and setting the stacking sequence for each element, which is not feasible.

4.3 The API program

4.3.1 Introduction to the API

The aforementioned limitations can be readily overcome with an Application Programming Interface (API) script. As FEMAP has its own library of API commands, it is possible to write a script that can automatically create individual property cards for each element, allowing the assignment of any fiber orientation for any ply. Before writing the API script, it should be emphasized that the program must be compatible with the MUL2@GL plug-in, which in practice means that 2D square laminate plate elements should be used.

4.3.2 Breakdown of the program

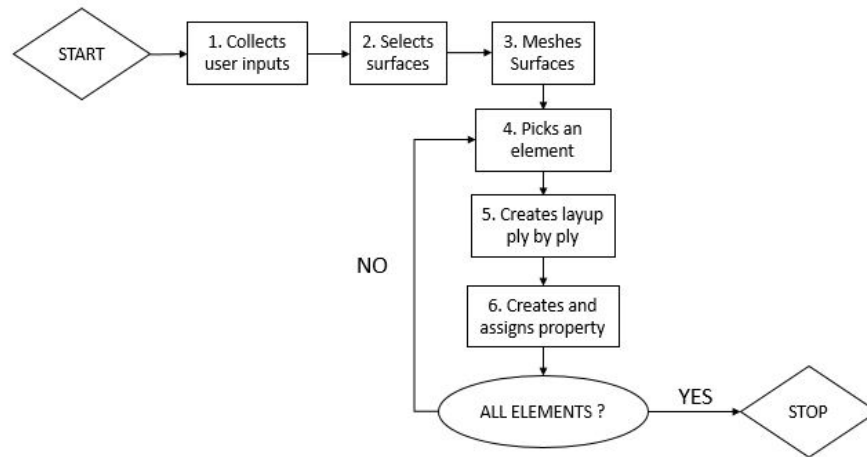
The API program is able to automatically generate a PCOMP card for each element by following user inputs. From a big-picture perspective the program can be summarized by the following steps, which are also summarized in Figure 4.6:

- **Step 1 - Collection of user inputs.** The program prompts the user to input the quantity, the material ID, the thickness, the angular orientation of each ply, as well as, the mesh size.
- **Step 2 - Surfaces selection.** The program prompts the user to select the surfaces to mesh.
- **Step 3 - Surface Meshing.** The program meshes the surface.
- **Steps 4, 5, 6 - Element Loop.** The program runs through all the elements present in the surfaces that have been meshed and calculate the fiber orientation in its geometrical center. After these calculations are done, the program creates a property card for the element and assigns it.

As the element used in the mesh is a four-node square element, it does not possess a central node. Hence, the material properties are calculated at its center as it is shown in 4.7, which means that the fiber orientation of the laminate is obtained through Equations 4.3 and 4.4.

$$P_{center} = \frac{G_{1,(x,y)} + G_{3,(x,y)}}{2} \quad (4.3)$$

Figure 4.6: Diagram of the whole API program

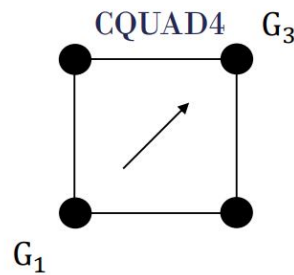


Source: The author

$$\theta_{x,y} = k_x x + k_y y + k \quad (4.4)$$

Where G_i are the coordinates of two opposing nodes and k_x , k_y and k are the coefficients of the angular function. Figure 4.7 shows the element and its G_1 and G_3 nodes as well as its orientation calculated at its center.

Figure 4.7: CQUAD4 element nodes indexing



Source: The author

4.4 The Local Model

The local model is built using the MUL2@GL tool developed by the MUL2 lab from Politecnico di Torino. This tool uses two main files as inputs, the bulk file which contains the NASTRAN cards which build the mesh, defining its material,

properties, nodes, elements, boundary conditions loading conditions, load cases and analysis types, and the results files, which basically contain the displacements. Once the desired element for the analysis is selected, these entries are internally treated in the MUL2@GL tool and the final outputs are the displacements, stresses, and strains of each ply for that specific element.

Chapter 5

Numerical Results

This chapter implements the theoretical formulations developed in the previous ones into software applications. The main goal is to validate the global-local workflow by comparing it to the results of other software and to other works in the literature. The implementation of the global model takes place in the FEMAP interface through the API program. Its nodal displacements and rotations are obtained with NASTRAN and are fed to the local model, which is created in the MUL2@GL plug-in. There are 3 case studies present, a thin plate under constant pressure, whose results are compared to those of an in-house 3D Layerwise program, a thick plate under the same loading condition, which is compared to the works of Demasi, and a thin plate under stretching, which is again compared to the LW software.

5.1 Thin Plate Bending

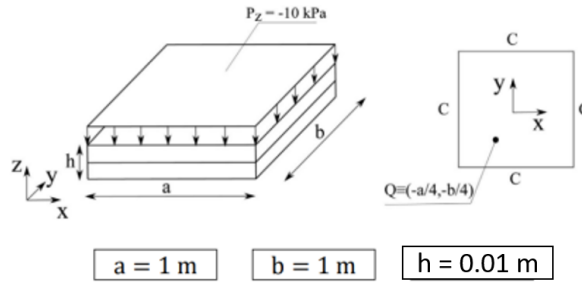
This section presents a simple case of a thin plate under bending. It is a starting point for the analysis of a VAT plate, because it has the least amount of complications as it is thin, only has two layers, one mechanical load, and a simple geometry with no stress concentrators. Its results are also very well known and behaved as it possesses an analytical solution. Therefore, it is an adequate first step for measuring the capabilities of the global-local workflow.

From a broad perspective, the analysis begins with a mesh convergence test to determine the refinement of the global and local meshes that produces the closest results to the benchmark. Once the mesh configuration is chosen, the next step is to plot the final interlaminar stresses and compare them to an in-house software that runs a full 3D layerwise model to get accurate results.

5.1.1 FEM Model

Starting with the description of the model, it consists in a thin plate with aspect ratio equals to 100. It is a 1 m square plate with 0.1 m thickness composed of 2 layers of a composite material, whose properties are shown in Figure 5.3. The fiber orientation, or rather, the lamination used in the plate is shown in Equation 5.1. The plate is clamped on all of its sides as represented by the letter C and subjected to a constant pressure of 10 kPa applied uniformly throughout its top surface. Figure 5.1 shows a sketch of the plate as well as its dimensions. The local results will be measured on point $Q = (-0.25, -0.25)$ m, and at point $C = (0.0, 0.0)$ with reference to the global coordinate system placed at the center of the plate.

Figure 5.1: Thin Plate under Bending

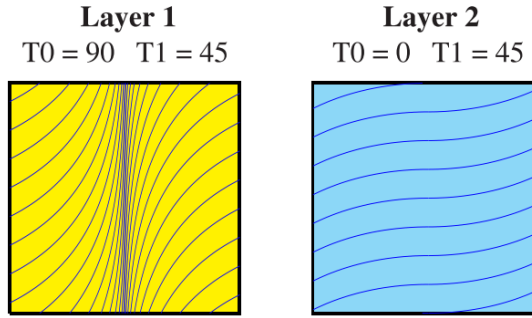


Source: The author

$$\left\{ \begin{array}{l} \theta_{x,y} = T_0 + \frac{T_1 - T_0}{d} |x| \\ \langle T_0^1, T_1^1 \rangle = \langle 90^\circ, 45^\circ \rangle \\ \langle T_0^2, T_1^2 \rangle = \langle 0^\circ, 45^\circ \rangle \\ d = 0.5 \text{ m} \end{array} \right. \quad (5.1)$$

Where the upper indexes T^k indicate the layer number and d refers to the half-length of the plate. The thickness is represented by $h = 0.01$ [m], the length is $a = 1$ [m], and the width is $b = 1$ [m]. A visual representation of this layup can be seen in Figure 5.2, where the orientation of the fibers for each layer is plotted on the plate. It is worth specifying that, $T_0^1 = 90^\circ$ refers to the fiber orientation at $x = 0$ of the plate for the first ply, and $T_1^1 = 45^\circ$ is the fiber orientation at $x = d = 0.05$ m. The same reasoning applies to T_0^2 and T_1^2 .

Figure 5.2: Thin Plate layup and fiber orientation



Source: [41]

Figure 5.3: Thin Plate Bending - General material properties

Material properties		Strength characteristics	
E_1 [GPa]	137.9	Z_T [MPa]	60.0
E_2, E_3 [GPa]	8.96	S_{13} [MPa]	174.54
G_{12}, G_{13} [GPa]	8.96	S_{23} [MPa]	152.66
G_{23} [GPa]	6.21	X_T [MPa]	2586.0
ν_{12}, ν_{13}	0.30	Y_T [MPa]	94.0
ν_{23}	0.49	S_{23} [MPa]	174.54

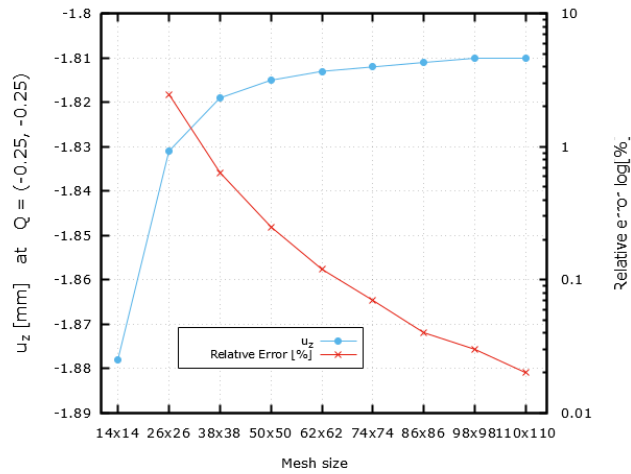
Source: [41]

5.1.2 Mesh Convergences

In a mesh convergence analysis, the main objective is to find a refinement more adequate for the study, which translates to finding an element size that provides accurate results in a manageable amount of time. This balance is usually found by solving the problem multiple times for increasingly finer mesh sizes to discover the sensibility of the results in relation to the refinement. This problem often proves to be rather difficult as the "true" results are not known. For this matter, there are various methods in the literature that propose stopping criteria for mesh convergences to help determine when the accuracy of the results is sufficient. In this work, the results are considered acceptable when the relative error goes below a certain threshold, which indicates that the physical quantity under evaluation is converging to a certain value. For a global-local approach, there are 3 ways in which the mesh can be refined, globally, locally in-plane, and locally out-of-plane. Hence, the strategy developed is to run a global convergence to determine the more adequate mesh and then proceed to the evaluation of the local one, in which the in-plane and the out-of-plane components are evaluated.

The global convergence is measured using the vertical displacement at $Q = (-0.25, -0.25)$ with a square mesh with increasing refinements ranging from 14×14 elements to as fine as 110×110 . Figure 5.4 shows u_z in function of the mesh sizes on the primary axis and the percentual relative error in logarithmic scale on the secondary axis. Its curves clearly show that the vertical displacement is tending to a certain value and at around 50×50 the error falls below 0.1%. Then at 110×110 the error is down to 0.02%, indicating that the value of u_z barely changed from the previous refinement and hence convergence is achieved. The next step is to find the

Figure 5.4: Thin Plate Bending - Global Convergence u_z

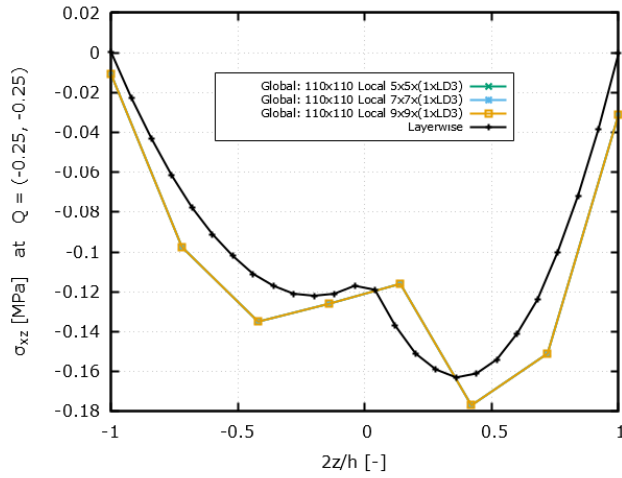


Source: The author

most appropriate size for the local mesh. Differently from the global one, the local is only tested for 3 distinct sizes, 5×5 , 7×7 , and 9×9 as further refinements could introduce problems that are discussed later in this work. The physical quantity chosen this time is the out-of-plane stress σ_{xz} as this type of stress is the main focus of the global-local approach. It was found that the results barely change in this analysis, hence instead of plotting the mesh convergence, Figure 5.5 shows a comparison between the σ_{xz} stresses for each of the refinements and it also plots the benchmark of the in-house Layerwise software. The vertical axis is the stress given in MPa and the x-axis is the normalized thickness of the plate $\frac{2z}{h}$. As can be seen, the three curves overlap each other, indicating that the results have already converged for the 5×5 size and further increments do not improve the results in a reasonable sense. It is also noted that the global-local curves are close to the LW ones.

The final test is to refine the out-of-plane mesh by using more LD3, which means using more interpolation points in the thickness, or rather more nodes. It is

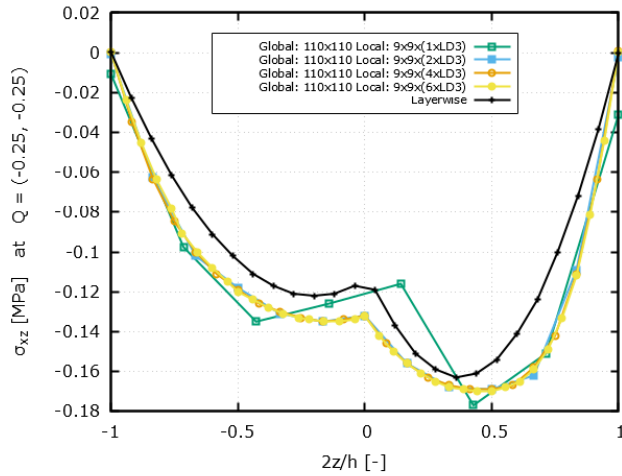
Figure 5.5: Thin Plate Bending - Local In-plane Convergence Comparison



Source: The author

highlighted that 1xLD3 is the minimum value for the analysis and that it already uses the best global mesh of 110×110 and the best local in-plane one of 9×9 . Figure

Figure 5.6: Thin Plate Bending - Local Out-of-plane Convergence Comparison



Source: The author

5.6 shows a comparison between the different number of through-the-thickness LD3 for σ_{xz} . As can be seen, the increase in interpolation nodes makes the curves look smoother, and more continuous. It is necessary to remark that this increase in discretization does not significantly improve the values of σ_{xz} at the middle of the

layers, but it provides a much better approximation to the layerwise benchmark at the ply's interfaces at $\frac{2z}{h} = 0$ and at the boundaries $\frac{|2z|}{h} = 1$, as the nodal computations are able to get closer to the boundary and represent its effects.

In summary, the configuration that yields the best results is the one that has 110×110 global mesh and $9 \times 9 \times 6$ LD3 local one and hence should be used in the general computation of the results comparison of the stress field.

5.1.3 Results Comparison

In this section, the results are compared to those computed by an in-house program, which uses 3D-elements for the calculation of the strain-stress field in all of the thin plate's domain using a Layerwise approach. This software is more accurate than the global-local approach proposed at the expense of longer computational times as it computes the interlaminar stresses for every element in the domain.

This comparison is carried out in two distinct points, $Q = (-0.25, -0.25)$ [m] and $C = (0.0, 0.0)$. Figures 5.7, 5.8, and 5.9 show the in-plane stress components in [MPa] at Q in function of the normalized thickness.

As can be seen, the results are quite close to the Layerwise ones. They are able to replicate the layer change at $\frac{2z}{h} = 0$, but suffer from a distortion in shape and at the boundaries. This effect is more pronounced in Figures 5.7 and 5.8 where the global-local curves diverge from curvilinear Layerwise ones especially at the top and bottom boundaries, $\frac{|2z|}{h} = 1.0$. These differences are discussed further in the chapter. The computation of in-plane shear σ_{xy} yields the best results as it overlaps the benchmark in its completeness.

The out-of-plane stresses are then represented by Figures 5.10 and 5.11. These results seem to replicate the general parabolic shape of the Layerwise ones as well as the discontinuity at the layer change. It is worth mentioning that differently from the in-plane results in Figures 5.7 and 5.8, the boundaries $\frac{|2z|}{h} = 1$ now match the benchmark, which was already expected, because in thin plates the through-the-thickness stress components, should be theoretically nill at the outer surfaces of the plate. Once more, the layer change at $\frac{2z}{h} = 0$ is replicated, even though the general shape of the global-local is wider than the LW benchmark.

It is also necessary to notice that the normal stress component σ_{zz} has not been provided because it is very prone to numerical errors. This is due to the fact that for the specific case of a thin plate under pure bending σ_{zz} is analytically nill for all points in the thickness, which causes the software computations to get very close to zero and to plot curves with lots of distortions, and no physical meaning.

Now that the results of point $Q = (-0.25, -0.25)$ have been discussed, it is important to check whether the global-local model is also compatible with other points in the plate, such as the one at the center of the plate, $C = (0.0, 0.0)$. It should be reminded that the numerical results in the plug-in are only calculated at

the very center of the element because it is the only Gaussian point for the chosen square element with 4 nodes. For this reason, the global mesh becomes 111×111 so that the center of the element matches exactly with point C . Figures 5.12, 5.13, and 5.14.

Differently from the results from point Q , in C there are no shape distortions for the in-plane stresses of Figures 5.12 or 5.13, only in the shear component 5.14 it is possible to observe a difference at the boundaries. Also, at the center of the plate the z -axis stresses σ_{xz} , σ_{yz} , and σ_{zz} are not shown for the same reason as before. For a thin plate, these stresses should be null at the plate center, as the plate undergoes pure 2D tension at this point, making the computation of out-of-plane components very prone to numerical errors and non-physical distortions.

Figure 5.7: EW Stress σ_{xx} at Q

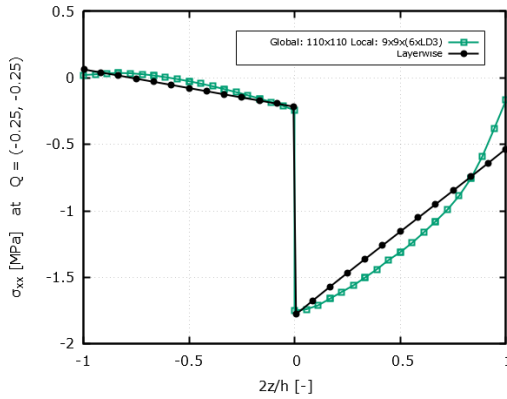


Figure 5.8: EW Stress σ_{yy} at Q

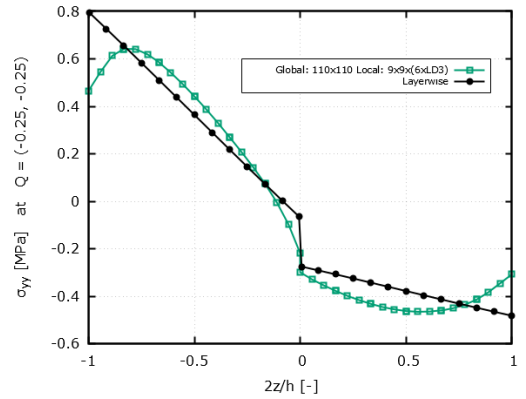


Figure 5.9: EW Stress σ_{xy} at Q

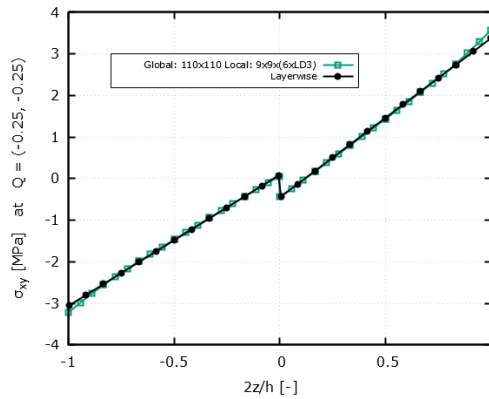


Figure 5.10: EW Stress σ_{xz} at Q

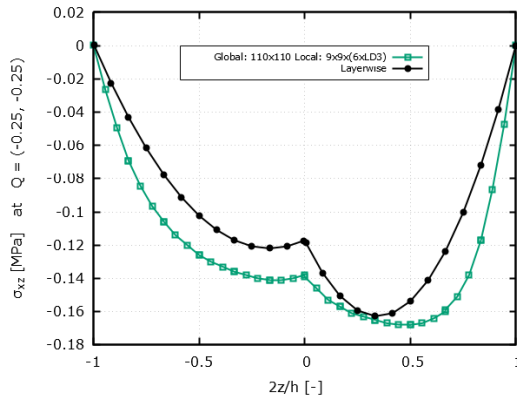


Figure 5.11: EW Stress σ_{yz} at Q

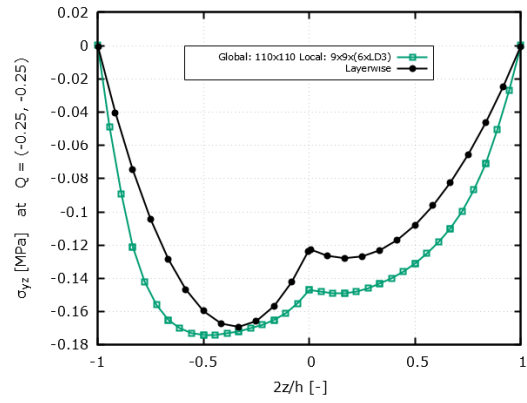


Figure 5.12: EW Stress σ_{xx} at C

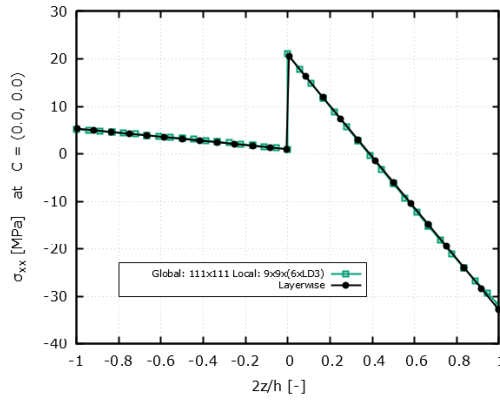


Figure 5.13: EW Stress σ_{yy} at C

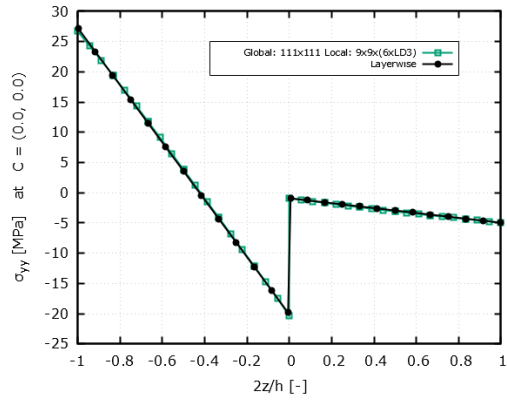
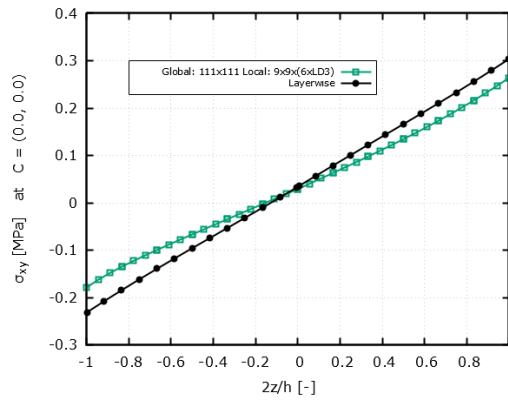


Figure 5.14: EW Stress σ_{xy} at C



5.1.4 Patch-wise Improvement

As could be seen in the previous section, the results are able to approximate the general shape of the Layerwise benchmark and are numerically close to them, but they still have room for improvement. The differences from the global-local results could be attributed to the fact that the interpolation of the local element does not have enough input data. It relies solely on the nodal displacements and rotations collected at the 4 interface nodes. To improve the results, it is possible to collect more information from the neighboring elements of the global model, or rather a patch of neighbor elements. In this way, the interpolation would have more parameters to work with and consequently the results would be improved, especially at the boundaries $\frac{|2z|}{h} = 1..$. This new approach is implemented by using a patch of 9 global elements, the center one being the one of interest, and the remaining 8 of its edge-sharing neighbors. Figures 5.15, 5.16, 5.17, 5.19, 5.18 show the new results with the Patch-wise (PW) approach while comparing them to the previous Element-wise (EW) as well as the Layerwise (LW) benchmarks.

It can be seen that the PW analysis is more accurate, as it superposes the LW approach even at the boundaries of the in-plane stresses, fixing the EW problems. Also, for the out-of-plane stresses the wider shape of the EW approach is narrowed with PW almost matching the LW curves.

This comparison is also repeated for point C in Figures 5.20, 5.21, and 5.22, where once again the PW results match the LW ones. The only component that has not overlapped its respective LW curve is σ_{xy} , but the overall second-degree behavior present in the EW curve is correctly fixed by PW, which is now linear like the PW stress. The results from the out-of-plane components of stress are once more not shown as they are too influenced by numerical errors as they approximate zero for every node along the thickness of the plate at point C .

Figure 5.15: PW Stress σ_{xx} at Q

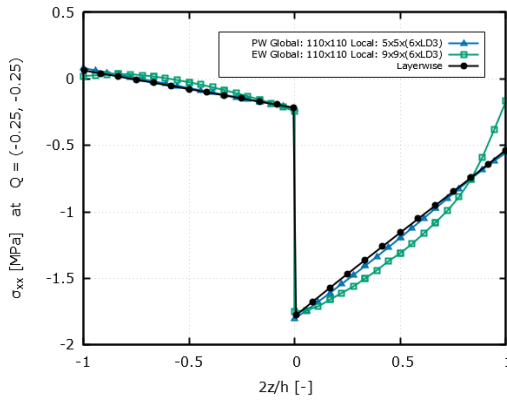


Figure 5.16: PW Stress σ_{yy} at Q

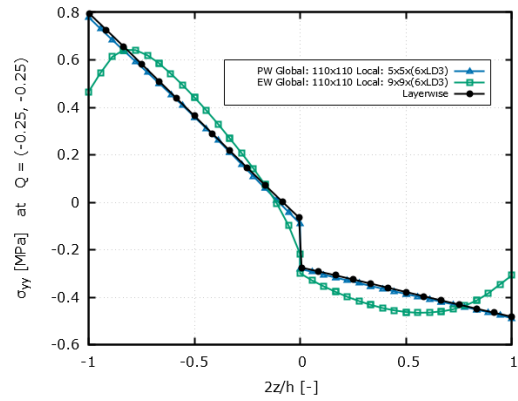


Figure 5.17: PW Stress σ_{xy} at Q

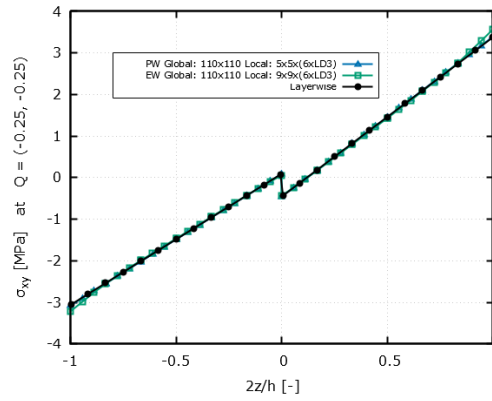


Figure 5.18: PW Stress σ_{xz} at Q

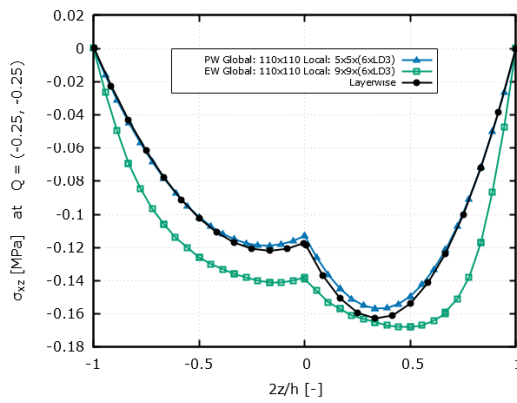


Figure 5.19: PW Stress σ_{yz} at Q

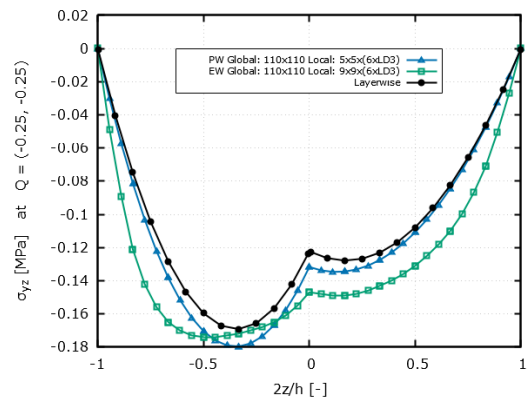


Figure 5.20: PW Stress σ_{xx} at C

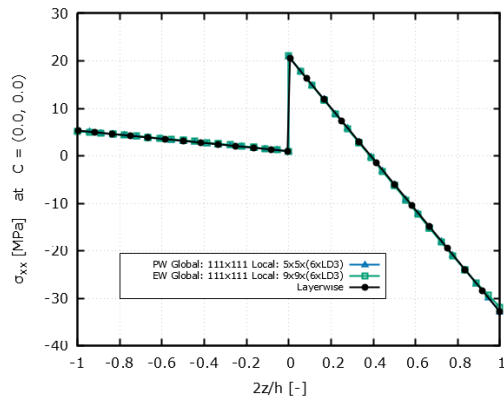


Figure 5.21: PW Stress σ_{yy} at C

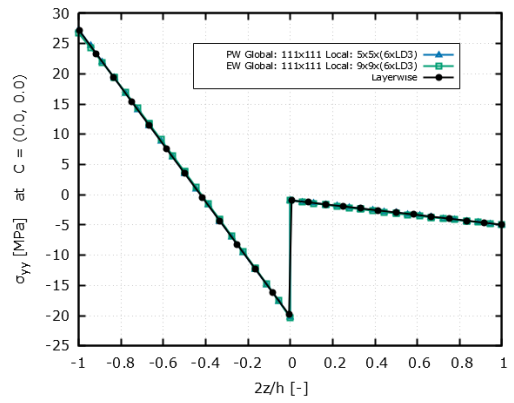
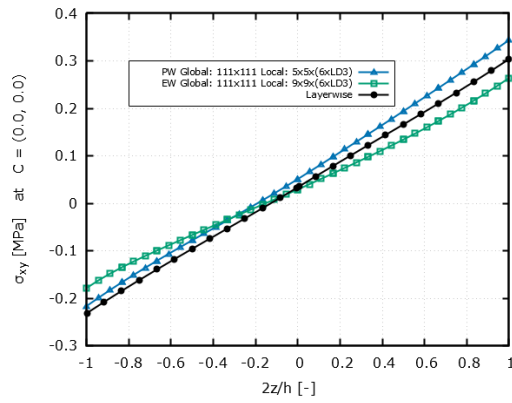


Figure 5.22: PW Stress σ_{xy} at C



5.1.5 Summary of the Thin Plate Bending

The conclusion is that the PW approach is able to achieve better results, which are not only numerically closer to LW, but also shape-wise. The addition of more global elements in the interpolation of the local ones did not make significant increases in the computation time but enabled the calculation of more accurate results, which is in line with the objective of this work. Both the EW and PW approaches are currently unable to replicate the PW benchmarks when regarding σ_{zz} for points Q and C as these values are very close to zero, although it is reminded that because these results are null, they would not be of interest in real engineering applications. Regarding σ_{xz} and σ_{yz} at point C , the results are simply not shown due to their proximity to zero and respective numerical errors. It is possible to affirm that the global-local model is capable of computing the interlaminar stresses of a thin VAT plate under static bending.

5.2 Thick Plate Bending

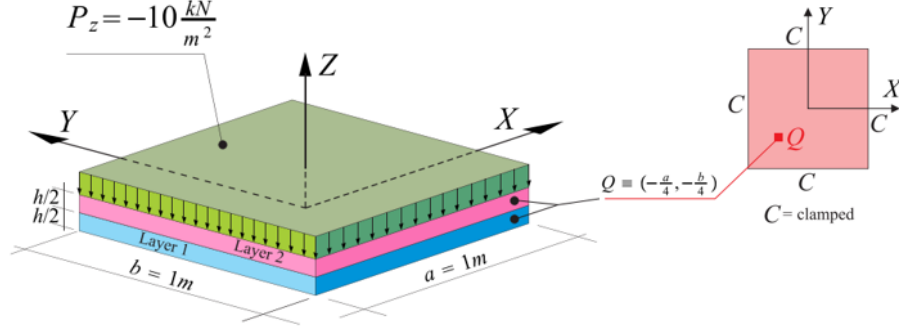
It would be desirable that the global-local workflow under development were able to also work for thick VAT plates, meaning for plates with an aspect ratio of more than 100 or at least close to 10. In this section, the boundaries to which the workflow can correctly model VAT plates are tested by introducing a plate very similar to the previous one to maintain a basis of comparison. The whole analysis procedure remains the same as for the thin plate, firstly a mesh convergence is performed to determine the best size configurations in terms of computational time and accuracy and secondly a comparison is made. It is remarked that the benchmark this time is not the in-house LW software, but the results from the work of [41].

5.2.1 FEM Model

The thick plate in this case is exactly the same as the thin one, with the exception of the thickness, which is 10 times higher. The material, lamination, loading, and boundary conditions remain the same. Hence, the model consists in a thick plate with aspect ratio equals 10, instead of the thin plate's 100. It is a 1 m square plate with 0.1 m thickness made of 2 layers of the same composite material. Its properties are repeated in Figure 5.25. The fiber orientation, or rather, the lamination used in the plate is shown in Equation 5.2 and does not differ from the thin one. The plate is clamped on all of its sides as represented by the letter C and subjected to a constant pressure of 10 kPa applied on its top surface. Figure 5.23 shows a sketch of the plate as well as its dimensions. The results will be measured on point

$Q = (-0.25, -0.25)$ m, and at point $C = (0.0, 0.0)$ with reference to the global coordinate system placed at the center of the plate.

Figure 5.23: Thick Plate under Bending



Source: [41]

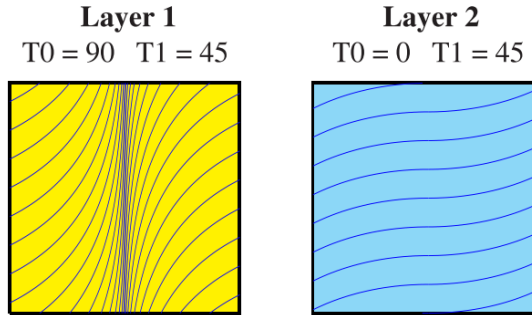
$$\left\{ \begin{array}{l} \theta_{x,y} = T_0 + \frac{T_1 - T_0}{d} |x| \\ \langle T_0^1, T_1^1 \rangle = \langle 90^\circ, 45^\circ \rangle \\ \langle T_0^2, T_1^2 \rangle = \langle 0^\circ, 45^\circ \rangle \\ d = 0.5 \text{ m} \end{array} \right. \quad (5.2)$$

Where the upper indexes T^k indicate the layer number and d refers to the half-length of the plate. The result of this layup can be seen in Figure 5.24, where the orientation of the fibers is plotted on the plate. It is worth specifying that, $T_0^1 = 90^\circ$ refers to the fiber orientation at $x = 0$ of the plate for the first ply, and $T_1^1 = 45^\circ$ is the fiber orientation at $x = d = 0.05\text{m}$. The same reasoning applies to T_0^2 and T_1^2 .

5.2.2 Mesh Convergences

To keep the similarities between the models of the thin plate and the thick one, most of the mesh convergences are maintained. The first step is the global convergence done by measuring the vertical displacement, the second step is to analyze the best in-plane local mesh, and the final step is to verify the ideal number of LD3 in the thickness.

Figure 5.24: Thick Plate layup and fiber orientation



Source: [41]

Figure 5.25: General material properties of the Thick Plate

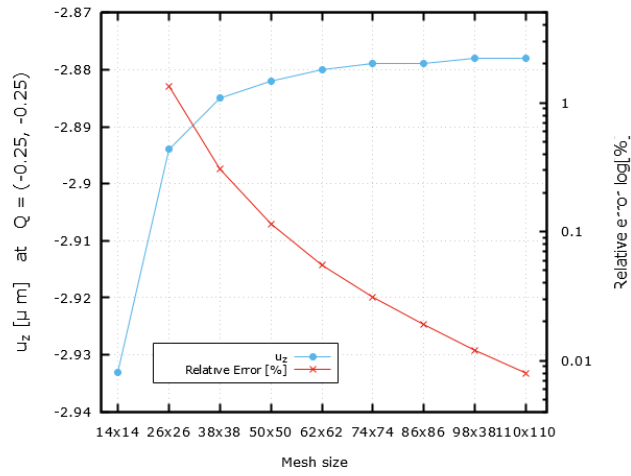
Material properties		Strength characteristics	
E_1 [GPa]	137.9	Z_T [MPa]	60.0
E_2, E_3 [GPa]	8.96	S_{13} [MPa]	174.54
G_{12}, G_{13} [GPa]	8.96	S_{23} [MPa]	152.66
G_{23} [GPa]	6.21	X_T [MPa]	2586.0
ν_{12}, ν_{13}	0.30	Y_T [MPa]	94.0
ν_{23}	0.49	S_{23} [MPa]	174.54

Source: [41]

Starting the battery of analyses, the global convergence measures the vertical displacement at $Q = (-0.25, -0.25)$ with a square mesh with increasing refinements ranging from 14×14 elements to as fine as 110×110 . Figure 5.4 shows u_z in function of the mesh sizes on the primary axis and the relative error in percentages on the secondary axis. The curves clearly show that the vertical displacement is converging to a certain value and at around 50×50 the error falls below 0.1% and at 110×110 the error is down to 0.008%, indicating that the value of u_z barely changed from the previous refinement and indeed the mesh has converged. This global convergence is notably similar to the thin plate one. The next step is to find the most appropriate size for the local mesh. Differently from the global one, the local is only tested for 3 sizes, 5×5 , 7×7 , and 9×9 , as further refinements could introduce some problems which are discussed later. The physical quantity chosen this time is the out-of-plane stress σ_{xz} as this type of stress is the main focus of the global-local approach.

To maintain the similarities of the thin plate analysis, Figure 5.27 shows the of σ_{xz} for all the sizes in comparison to the in-house Layerwise software. The vertical axis is the stress given in [MPa] and the x-axis is the normalized thickness of the

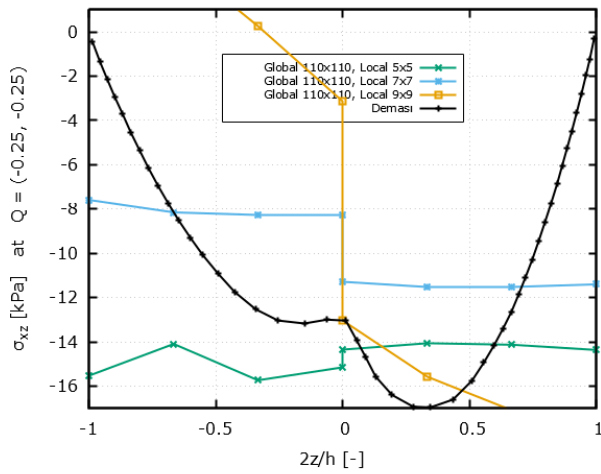
Figure 5.26: Thick Plate Bending - Global Convergence



Source: The author

plate $\frac{2z}{h}$. This time, the results are very poor. Even though the global mesh showed

Figure 5.27: Thick Plate Bending - Local In-plane Convergence Comparison



Source: The author

convergence, the local mesh provided results that do not appear to converge. In fact, the 5×5 mesh and the 7×7 one look flat and do not follow the parabolic curvature of the LW results. The only similarity between any of the different curves seems to be the discontinuity present at the layer change.

Upon further investigation, the poor quality of the results is attributed to the

aspect ratio of the local element. Having a thicker plate, but using the same global mesh means that the local element would have a thickness much higher than its characteristic length, which would violate any premises of a thin or thick plate theory. In fact, the aspect ratio of the local element in the thin plate case for a 110×110 global mesh and 9×9 local one would be given by Equation 5.3:

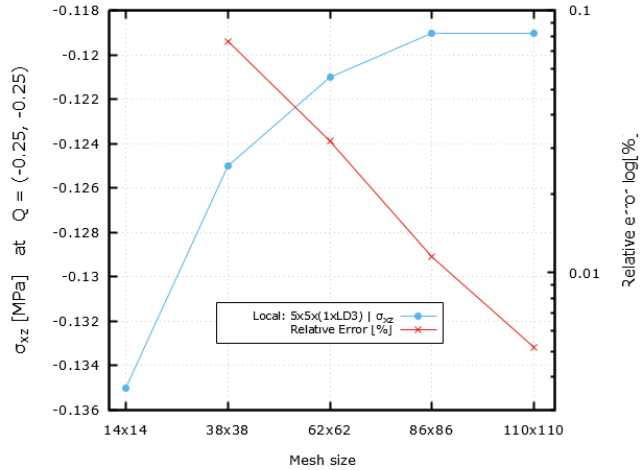
$$\frac{t_{thin}}{h_{thin}} = \frac{0.01}{\frac{1}{110 \cdot 9}} = 9.9 \quad (5.3)$$

And the aspect ratio for the thick plate in the same conditions would be given by Equation 5.4:

$$\frac{t_{thick}}{h_{thick}} = \frac{0.1}{\frac{1}{110 \cdot 9}} = 99 \quad (5.4)$$

Which is indeed 10 times higher than the thin plate's one. In light of this information, another mesh convergence analysis is performed, but instead of considering the vertical displacement u_z , the σ_{xz} stress component is directly used, in order to understand the sensibility of the stress component against the global mesh. Figure 5.28 shows the convergence analysis for increasing refinements of the global mesh from 14×14 to 110×110 for σ_{xz} .

Figure 5.28: Thick Plate Bending - Local In-plane Convergence

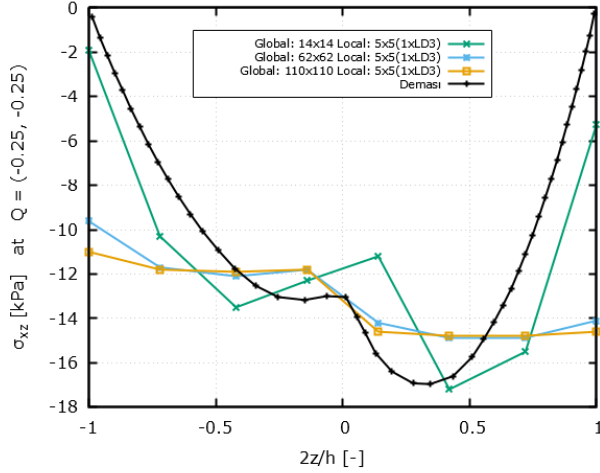


Source: The author

Once again the results seem to converge for the more refined meshes, such as 86×86 and 110×110 , but as has been previously observed, the comparison to LW in Figure 5.27 shows that the stress plot is not good. Hence, another comparison is made. The comparison done in Figure 5.29 uses a 14×14 mesh, to attempt to

match the aspect ratio of the thin plate from Equation 5.3. Using this refinement yields a much closer aspect ratio of $\frac{t}{h} = 13.6$.

Figure 5.29: Thick Plate Bending - Local Convergence Comparison



Source: The author

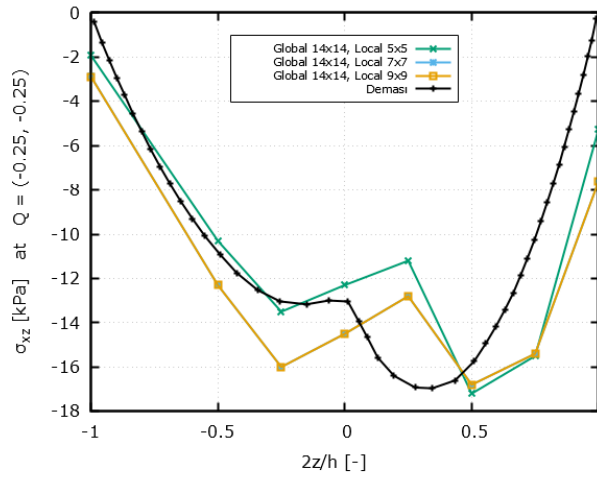
From Figure 5.29 it is observed that the 14×14 mesh is indeed the closest to LW and the finer ones are worse and worse. With this comparison it becomes clear that very high aspect ratios originating from finer meshes such as 62×62 and 110×110 drive the calculations out of the scope of the theoretical premises, resulting in poor quality results. Using a 14×14 mesh it is possible to repeat the test from 5.27. Figure 5.30 shows the local in-plane mesh comparison for the coarser mesh of 14×14 .

Hence, it is found that the most suitable local in-plane mesh should be 9×9 . It is worth mentioning that the σ_{xz} already converges for 7×7 , but 9×9 is chosen to maintain some parallelism with the thin plate case and the computational time was not increased significantly.

The final test is to refine the out-of-plane mesh by using more LD3, which means using more interpolation points in the thickness per layer. It is worth mentioning that 1LD3 is the default value for the analysis and that the analysis incorporates the best global mesh of 14×14 and the best local in-plane one of 9×9 .

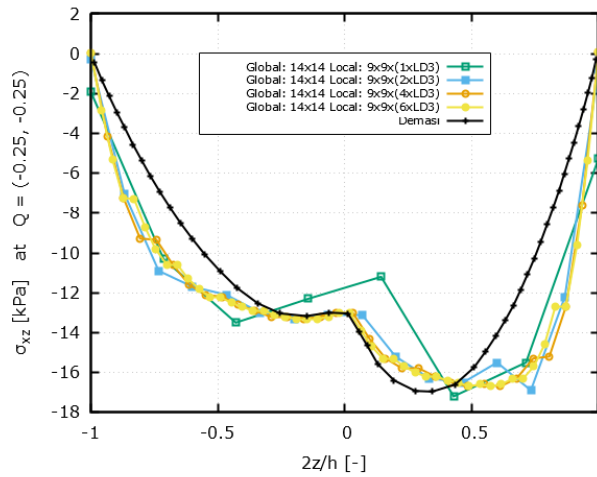
Just like for the thin plate of Figure 5.6, Figure 5.31 shows a comparison between the different refinements for σ_{xz} . The increase in interpolation nodes makes the curves look smoother, more continuous. It is necessary to remark that the values of σ_{xz} do not change much in the middle of the layers, they show a much better approximation to the layerwise benchmark at the plies' interfaces at $\frac{2z}{h} = 0$, and at the boundaries $\frac{|2z|}{h} = 1$.

Figure 5.30: Thick Plate Bending - Local Convergence Comparison



Source: The author

Figure 5.31: Thin Plate Bending - Local Out-of-plane Convergence Comparison



Source: The author

In summary, the configuration that yields the best results is the one that has 14×14 global mesh and $9 \times 9 \times 6xLD3$ local one and hence should be used in the general computation in the results comparison of the stress field. It must also be noted that by using a 14×14 global mesh, the results are no longer as accurate as if a 110×110 were used and as Figure 5.28 shows, the coarser mesh has a difference in σ_{xz} of around 13% in comparison to the finer one.

5.2.3 Results Comparison

In this section, the results are compared to those computed by [41], who uses 3D elements for the calculation of the strain-stress field in all of the thick plate using a PVD approach. The results are compared only in point $Q = (-0.25, -0.25)$ m. The first comparison is done for the vertical displacements in Figure 5.32, whose benchmark results are from [41] that compares LD2, LD3 and high-order 3D elements for the global mesh. Where the LD2 results are of second-order 3D

Figure 5.32: Comparison of vertical displacements

	LD2	LD3	Demasi et al	NASTRAN
uz E+6 [m]	-2.84	-2.89	-2.81	-2.94
Relative Difference (%)	3.5%	1.7%	4.6%	-

Source: The author

elements, LD3 results are of third-order 3D elements and Demasi's results are of high-order 3D elements, while the NASTRAN results only used first-order 2D elements. As the comparison shows, the vertical displacements from NASTRAN's global model are very similar to those found in the reference as the highest relative difference is at 4.6% in comparison to a high-order model. It is worth mentioning that although the NASTRAN results come from a relatively coarse 14×14 mesh the results are still quite good and this relative difference would be even lower if the global mesh used were 110×110 . Figures 5.33, 5.34, and 5.35 show the in-plane stress components in [MPa] at Q in function of the normalized thickness. As can be seen, the results are not so close to the Layerwise ones. Despite having the same order of magnitude, they show the same problem as in the thin plate results. The global-local curves are distorted at the boundaries. Furthermore, 5.34 does not match LW in regards to the layer discontinuity. This problem is addressed further in this chapter with the PW improvement. Next, Figures 5.36 and 5.37 represent the out-of-plane stresses.

The results here are better than the in-plane ones and seem to replicate the general parabolic shape of the Layerwise ones, but still show some degree of distortion. It is worth mentioning that differently from the in-plane results the boundaries $\frac{|2z|}{h} = 1$. now match the benchmark, which was already expected, because in plates the through-the-thickness stress components, meaning the stresses on the outer surfaces, should be null. Once again, the layer change at $\frac{2z}{h} = 0$. is replicated, even though the general shape of the global-local is wider than the benchmark. It is also necessary to notice that the normal stress component σ_{zz} has not been provided again, because it was very prone to numerical errors. This is due to the fact that for the specific case of a thin plate under pure bending σ_{zz} is

Figure 5.33: EW Stress σ_{xx} at Q

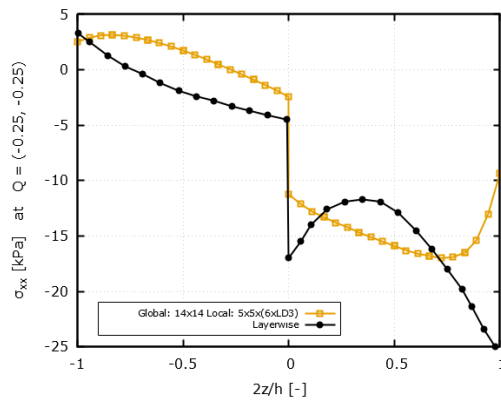


Figure 5.34: EW Stress σ_{yy} at Q

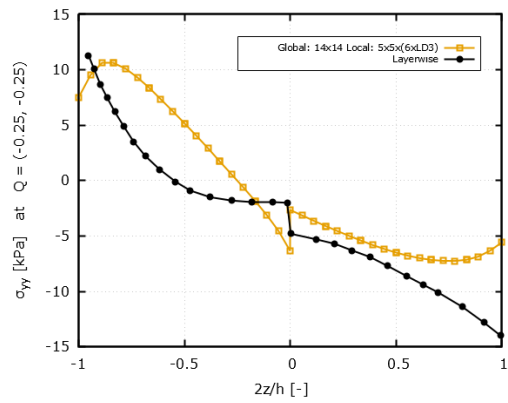


Figure 5.35: EW Stress σ_{xy} at Q

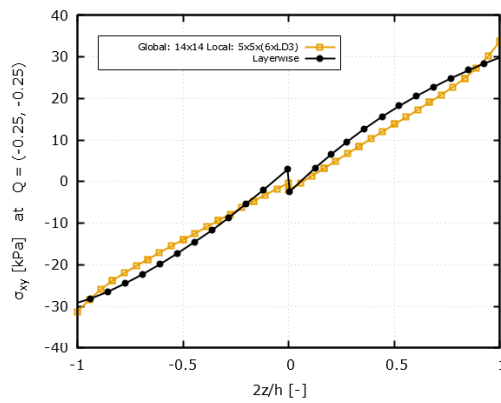


Figure 5.36: EW Stress σ_{xz} at Q

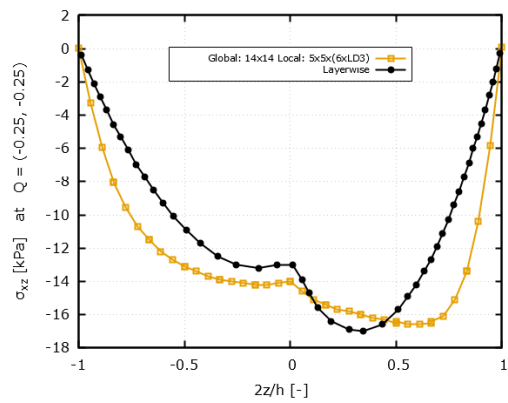
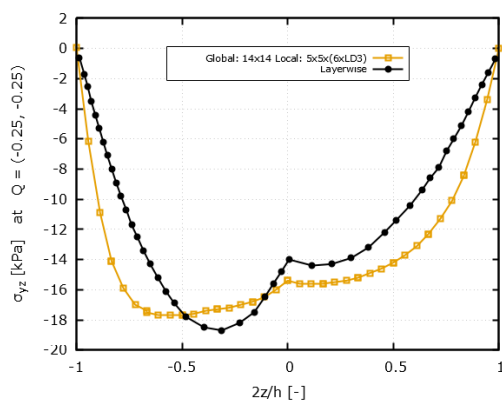


Figure 5.37: EW Stress σ_{yz} at Q



analytically null, which causes the software computations to get very close to zero and to plot curves with lots of distortions, and hence no physical meaning.

5.2.4 Patchwise Improvement

In the same manner, as for the thin plate, the results are able to approximate the general shape of the Layerwise benchmark and are numerically close to them, but they still have room for improvement. The differences from the global-local results could be attributed to the fact that the interpolation of the local element does not have enough input data. It relies solely on the nodal displacements and rotations collected at the 4 interface nodes. To improve the results, the Patch-wise analysis is repeated for the thick plate. In this way, the interpolation would have more parameters to work with and consequently improve the results, especially at the boundaries $\frac{|2z|}{h} = 1..$ This approach is implemented by using a patch of 9 global elements, the center one being the one of interest, and the remaining 8 its edge-sharing neighbors. It is worth mentioning that these 9 elements are further divided into 9×9 local elements. Figures 5.38, 5.39, 5.40, 5.42, 5.41 show the new results with the Patch-wise (PW) approach while comparing them to the previous Element-wise (EW) and the Layerwise (LW) benchmarks.

As can be seen, the PW analysis is more accurate, it superposes the LW approach even at the boundaries, especially for the in-plane stresses. Also, for the out-of-plane stresses the general wider shape of the EW approach is fixed with PW, it resembles the LW benchmark more closely. Furthermore, even the out-of-plane stress σ_{zz} can now be accurately represented, confirming that the PW results indeed produce better results.

5.2.5 Summary of the Thick Plate Bending

Unlike the thin plate, the thick plate under bending requires a better understanding of the sensibility of the mesh size. The results are improved by further refinements of the global mesh, but a lot of attention must be paid to the aspect ratio of the local element, as a small element with a correlated high aspect ratio can introduce border effects that distort the stress curves and are dominated by numerical errors. Better quality results are obtained by maintaining the aspect ratio close to 10, matching the one from the thin plate. The results closest to the reference are obtained with a global mesh of 14×14 and a local one of $9 \times 9 \times 6LD3$ with the use of the PW approach.

Figure 5.38: PW Stress σ_{xx} at Q

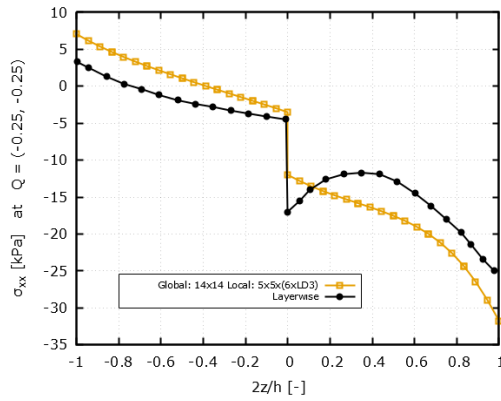


Figure 5.39: PW Stress σ_{yy} at Q

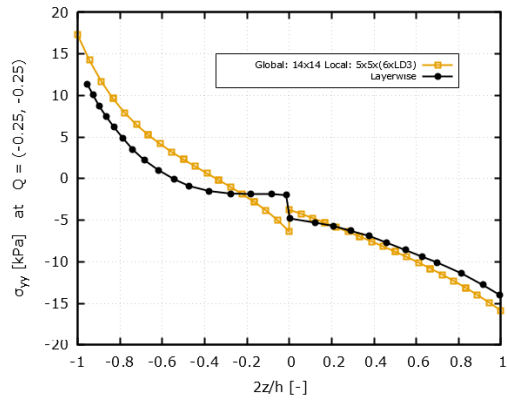


Figure 5.40: PW Stress σ_{xy} at Q

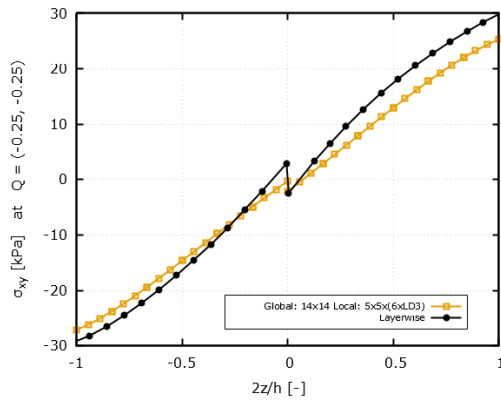


Figure 5.41: PW Stress σ_{xz} at Q

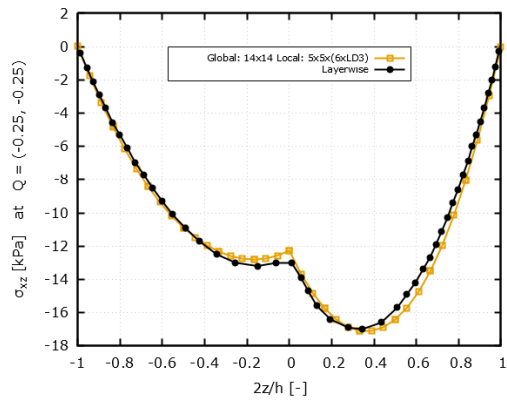


Figure 5.42: PW Stress σ_{yz} at Q

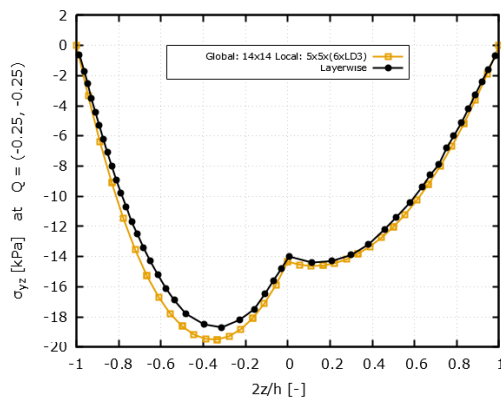
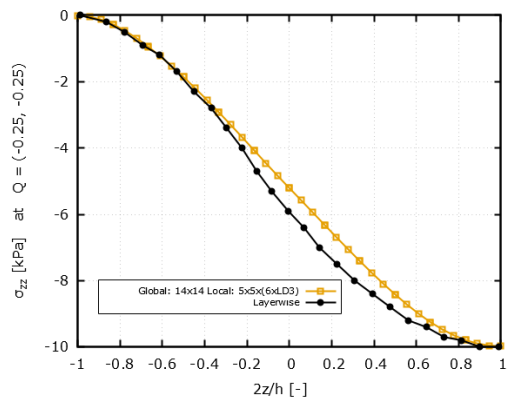


Figure 5.43: PW Stress σ_{zz} at Q



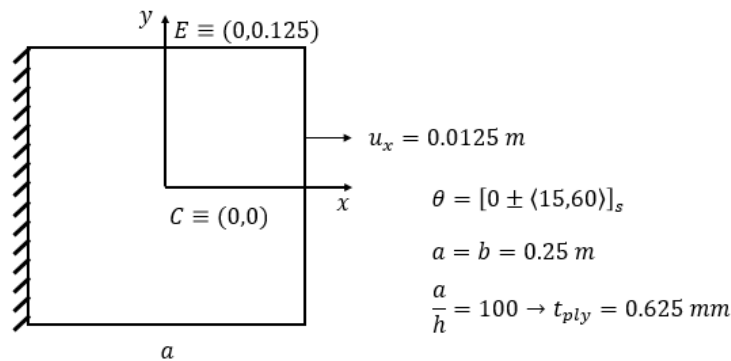
5.3 Thin Plate Stretching

In this section, some alterations are made to allow the computation and further comparison of free-edge stresses. This type of analysis is of interest because anisotropic laminates that are subject to humidity, temperature, or mechanical loads develop a distinct form of failure that is characterized by a severe strain concentration at a narrow boundary region nearing their free-edge, which usually leads to the delamination and further failure of the composite. This problem is quite complex and many commercial software are not able to compute them. NASTRAN for example does not take free-edge stresses into account when dealing with laminates, but the MUL2@GL plug-in does.

5.3.1 FEM Model

As the previous thin and thick plates were both clamped on all of its edges there were no free-edge effects, so in this example, the plate is clamped only on its left edge and pulled with a constant displacement of $u_x = 0.0125$ [m] on its right edge. Also, the lamination is changed to a symmetric one described by Equation 5.5 to further test the global-local workflow. The only detail that remains unchanged from the two previous plate examples is the material properties table, in Figure 5.45. Two points are chosen for the analysis, point $C = (0.0, 0.0)$ at the plate's center and $E = (0, 0.125)$ at the top edge. The first is used as means to check whether the MUL2@GL plug-in works for this new configuration of geometry, load case, and lamination. The latter is where the free-edge effects are prominent and should be computed. Figure 5.44 shows a brief sketch of the thin plate under stretching and its computation points, as well as details of its lamination. Where a , b , h , and

Figure 5.44: Thin Plate under Stretching model



Source: The author

t_{ply} are the length, width, thickness, and ply thickness of the plate, respectively.

Figure 5.45: Material properties of the Thin Plate under Stretching

Material properties		Strength characteristics	
E_1 [GPa]	137.9	Z_T [MPa]	60.0
E_2, E_3 [GPa]	8.96	S_{13} [MPa]	174.54
G_{12}, G_{13} [GPa]	8.96	S_{23} [MPa]	152.66
G_{23} [GPa]	6.21	X_T [MPa]	2586.0
ν_{12}, ν_{13}	0.30	Y_T [MPa]	94.0
ν_{23}	0.49	S_{23} [MPa]	174.54

Source: The author

$$\left\{ \begin{array}{l} \theta_{x,y} = T_0 + \frac{T_1 - T_0}{d} |x| \\ \langle T_0^1, T_1^1 \rangle = \langle 15^\circ, 60^\circ \rangle = \langle T_0^4, T_1^4 \rangle \\ \langle T_0^2, T_1^2 \rangle = \langle -15^\circ, -60^\circ \rangle = \langle T_0^3, T_1^3 \rangle \\ d = 0.125 \text{ m} \end{array} \right. \quad (5.5)$$

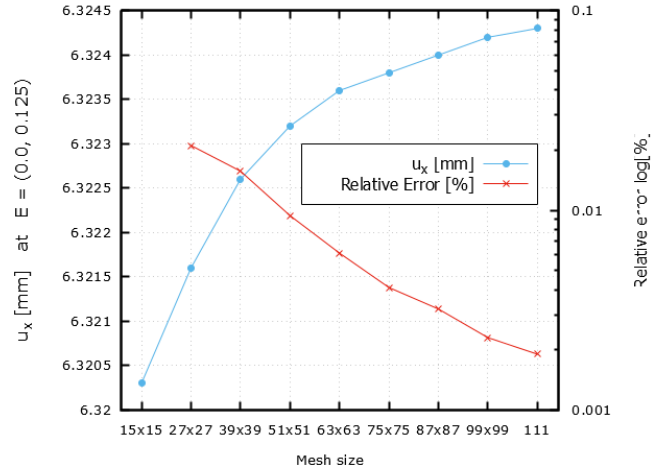
It is worth highlighting that the laminate in question is symmetric as the first and fourth layers have the same fiber orientation as well as the second and third, which means that the in-plane stresses computed later in the section should all be symmetric in respect to the midplane of the plate.

5.3.2 Mesh Convergences

As usual, the mesh convergences are composed of three consecutive parts, a global one, a local in-plane one, and a local out-of-plane one. As this model does not possess vertical displacements, due to the nature of the loading cases and boundary conditions, the first convergence is measured with the in-plane displacements u_x and u_y to guarantee the accuracy of the global model. As the main objective here is to compute the free-edge stresses, the mesh convergence is measured at point $E = (0.0, 0.125)$ [m] rather than any other point in the plate.

As depicted in Figure 5.46, the x -displacement already shows relative errors in the order of 0.02% in the very first refinement from 15×15 to 27×27 and it continues to decrease until 0.002% for the 111×111 mesh. The usual inverse negative exponential curve of u_x alongside the decreasing relative error indicates that global convergence has been reached. In the same way as u_x , u_y also shows a convergent pattern. Figure 5.47 shows that the secondary axis displacement has a 1% relative error for the first iteration at 27×27 , which further decreases to 0.01%

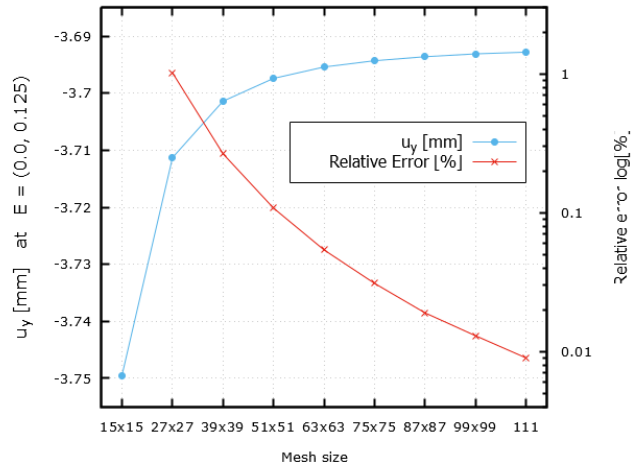
Figure 5.46: Thin Plate Stretching - Global Convergence u_x



Source: The author

at the 111×111 global mesh. The displacement curve also has the exponential pattern which indicates convergence. As the relative error is low for both in-plane displacements u_x and u_y even for the very first mesh refinements, it is possible to say that any mesh within the considered range of 15×15 to 111×111 may produce acceptable results from a global perspective. As previously observed in the thick

Figure 5.47: Thin Plate Stretching - Global Convergence u_y

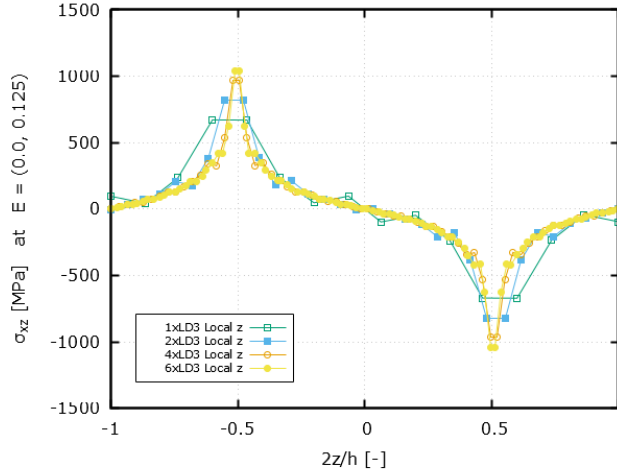


Source: The author

plate section, the achievement of global convergence in the model is not enough to

guarantee acceptable results, as a too-refined model results in local elements with aspect ratios outside the domain of plate theory. For the free-edge the local in-plane convergence also shows a very high sensibility to alterations in the refinement, meaning that the usual 5×5 , 7×7 , and 9×9 local meshes provided very inconsistent results. For this reason, this analysis is not shown. Conversely, the out-of-plane convergence in Figure 5.48 shows results consistent with previous sections. As

Figure 5.48: Thin Plate Stretching - Global Convergence u_y



Source: The author

can be seen on Figure 5.48, the increasing number of LD3 used in the thickness provides smoother curves, which also begin to reveal a peak in σ_{xz} stress as the computational nodes approach the layer transition in $\frac{2z}{h} = -0.5$ and in $\frac{2z}{h} = 0.5$ as the out-of-plane nodes are computed closer to the boundaries for an increasing number of LD3 in the model.

5.3.3 Results Comparison

In this section, the results are once again compared to the in-house LW software, the same used for the thin plate under bending case. As has been previously mentioned, mesh convergence for the local element is particularly difficult to find, because the local mesh is very influential in these computations, therefore many configurations of global and local refinements are tested and among these many ones, the 13×13 global mesh and $5 \times 5 \times 2$ LD3 local one provide the results closest to the LW benchmark for point C , but for the free-edge point E , the best combination was 63×63 global mesh and $7 \times 7 \times 2$ LD3 local. This indicates that the free-edge effects need a more refined global mesh to correctly calculate its effects. It is important to highlight that the 2LD3 configuration is chosen because more LD3 per

layer would pollute the graphics with too many points, making them harder to read, also it is found that the use of 6LD3 for this scenario would only make the curves smoother and not produce a significant improvement in the stress computations.

Figures 5.49, 5.50, and 5.51 show the in-plane stresses calculated at point $C = (0.0, 0.0)$ in function of the normalized thickness. The out-of-plane stresses are not shown, because they all tend to zero and hence are subject to numerical errors and possess little to no physical relevance.

It is possible to see that Figures 5.49 and 5.50 are quite flat, indicating that the stress distribution along the thickness of the plate is approximately constant, which was expected since a unidirectional edge pull should produce a rather uniform tension among the cross-section of a thin plate. Nevertheless, the tensions σ_{xx} and σ_{xy} are not perfectly constant through the thickness as there are discontinuities at the layer transitions at $\frac{|2z|}{h} = 0.5$. Figure 5.51 accurately depicts the effect of the symmetric layup as σ_{xy} is positive in the first and last layers, which share the same fiber orientation, and negative for the middle layers. It is further remarked that there is no noticeable transition at $\frac{2z}{h} = 0.0$, because the fibers have the same orientation in the third and second layers.

Next, the computations are made at the free-edge point $E = (0.0, 0.125)$. Figures 5.52, 5.53, and 5.54 show the in-plane stresses for this point in function of the normalized thickness. It is noted that for the out-of-plane stresses σ_{xz} and σ_{yz} become significant in the free edge and are therefore evaluated.

In Figures 5.52, 5.53, and 5.54 it is possible to observe that the global-local plug-in produces results quite close to those of the benchmark, especially for the shear stress σ_{xy} . When it comes to σ_{xx} and σ_{yy} the global-local curves seem to represent the general shape of the LW software, except for the middle part $\frac{|2z|}{h} \leq 0.5$, where they have opposing curvature. It is highlighted that even though σ_{yy} is 2 orders of magnitude lower than the other in-plane components σ_{xx} and σ_{xy} , its global-local curve visually approximates the LW benchmark, albeit with a high relative error.

Next, Figures 5.55 and 5.56 present the out-of-plane stresses. Once again, it is reminded that the σ_{zz} is not shown because its values approach zero and the computations are heavily affected by numerical errors.

Upon observation, the out-of-plane stresses from Figures 5.55 and 5.56 do not match their respective benchmarks. The differences in the σ_{yz} stress component could be attributed to numerical errors since it is orders of magnitude lower than the ones, but the same can not be said about σ_{xz} , which appears to be flat in comparison to the benchmark and does not seem to have a similar shape in the sense that the noticeable layer transition present in the LW benchmark is not seen in the global-local curve.

Figure 5.49: EW Stress σ_{xx} at C

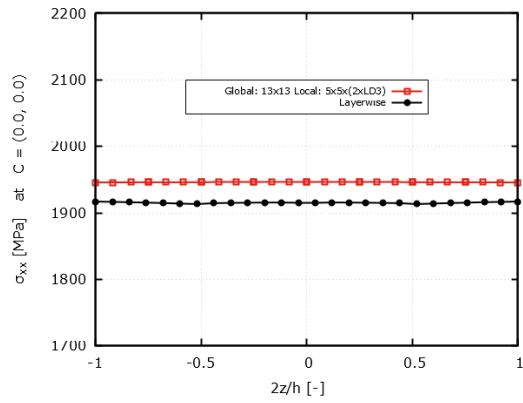


Figure 5.50: EW Stress σ_{yy} at C

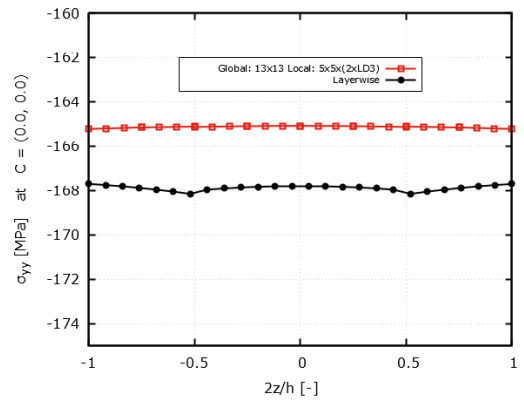


Figure 5.51: EW Stress σ_{xy} at C

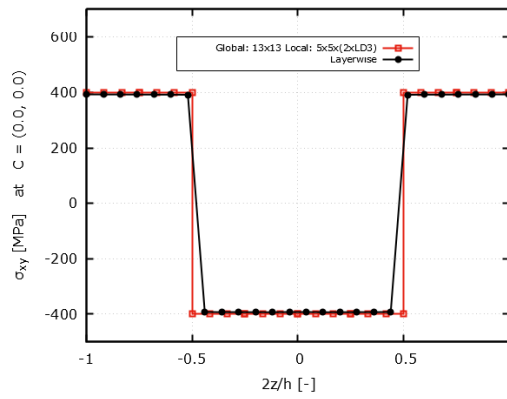


Figure 5.52: EW Stress σ_{xx} at E

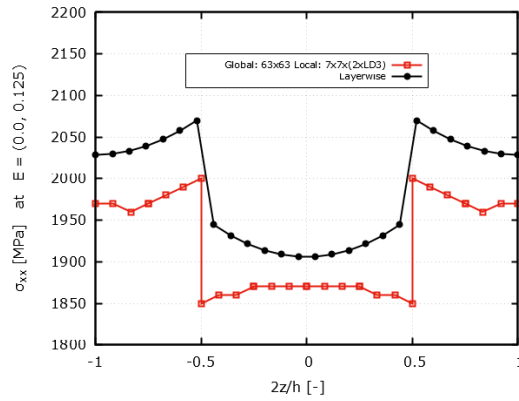


Figure 5.53: EW Stress σ_{yy} at E

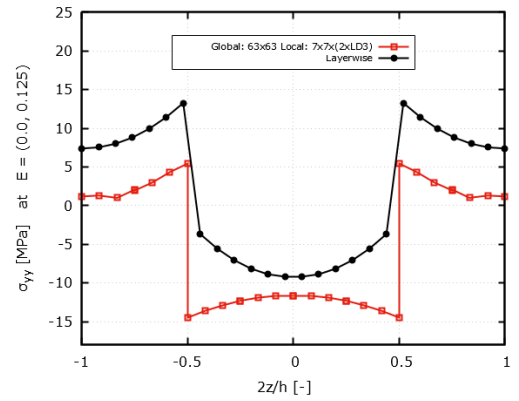


Figure 5.54: EW Stress σ_{xy} at E

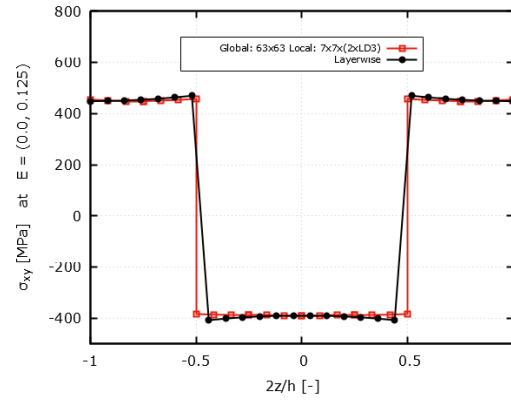


Figure 5.55: EW Stress σ_{xz} at E

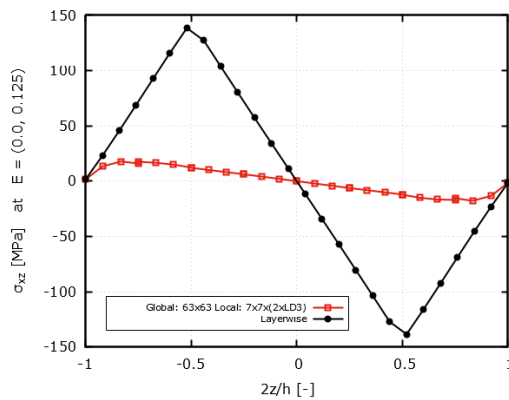
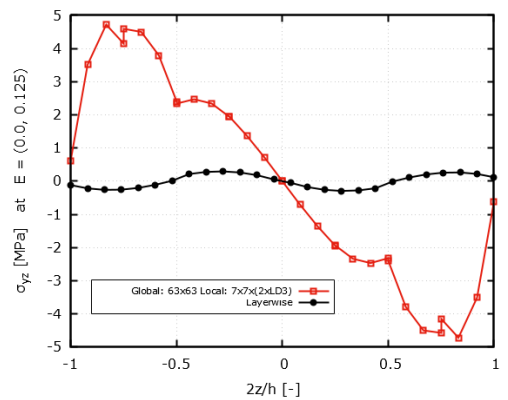


Figure 5.56: EW Stress σ_{yz} at E



5.3.4 Patch-wise Improvement

Given the dissimilarities from the out-of-plane stresses with their respective benchmarks, the Patch-wise approach aims to introduce more input points to the local model and therefore to improve the numerical interpolation within the local model. Figures 5.57, 5.58, and 5.59 compare the PW stresses with the EW ones for point C . It is found, albeit not shown, that the PW results for a 13×13 global mesh are not satisfactory, instead, the stresses computation works best for a PW with a global mesh of 63×63 and $5 \times 5 \times 2LD3$, which is put in direct comparison to the EW 13×13 and $5 \times 5 \times 2LD3$ mesh results.

As can be seen in the EW-PW comparison, the results of the latter do not show the same significant improvement that is observed for the thin and thick plates under bending. While there is an improvement in the computation of σ_{yy} , there is a deterioration in both σ_{xx} and σ_{xy} , therefore it is concluded that the PW approach has not been fruitful for the stress computations at point C .

At the free edge, the results have also not improved by a significant margin. Figures 5.60, 5.61, and 5.62 show the in-plane stresses at the free-edge.

As the graphics show, the PW approach has also not improved the computations, in fact, all three σ_{xx} , σ_{yy} , and σ_{xy} have moved farther away from the benchmark, especially σ_{yy} in Figure 5.61. Lastly, the out-of-plane stresses are computed in Figures 5.63 and 5.64.

Once again, the PW does not show signs of improvement. In Figure 5.64 the order of magnitude of σ_{yz} is significantly lowered from EW to PW, but it is still drastically different from the benchmark. In Figure 5.63 the results are also not improved.

Figure 5.57: PW Stress σ_{xx} at C

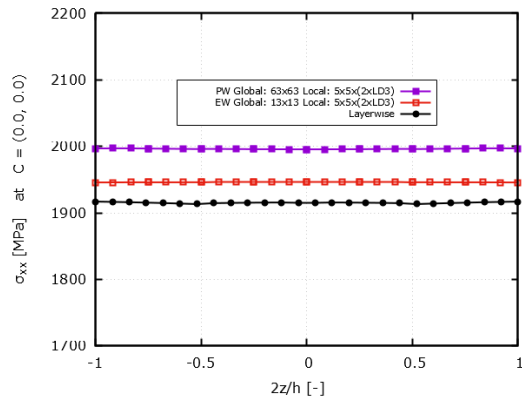


Figure 5.58: PW Stress σ_{yy} at C

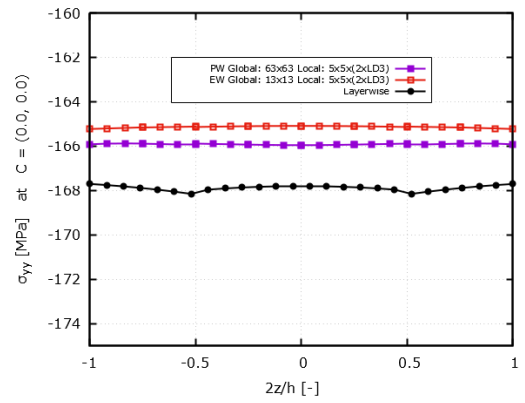


Figure 5.59: PW Stress σ_{xy} at C

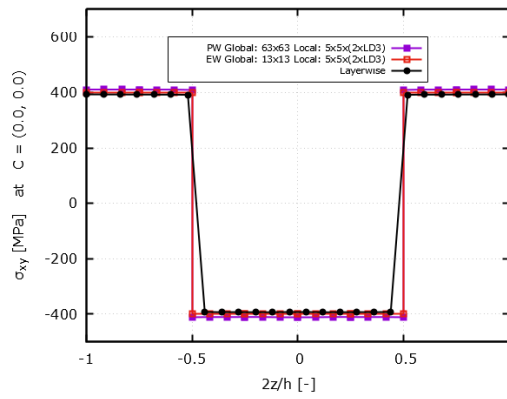


Figure 5.60: PW Stress σ_{xx} at E

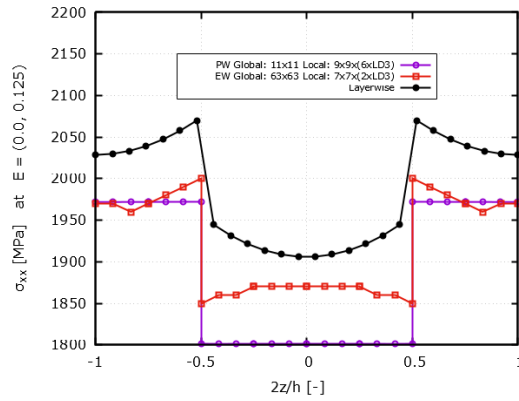


Figure 5.61: PW Stress σ_{yy} at E

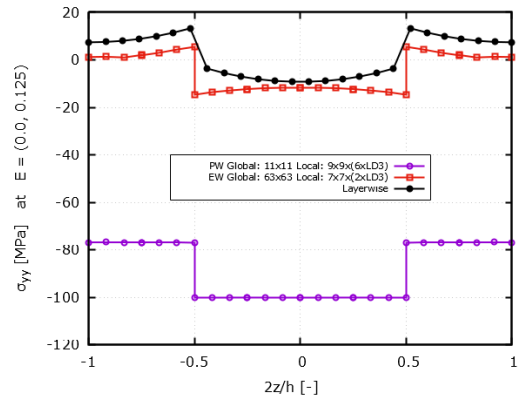


Figure 5.62: PW Stress σ_{xy} at E

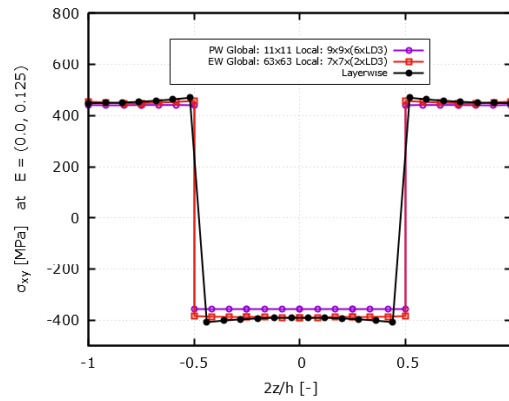


Figure 5.63: PW Stress σ_{xz} at E

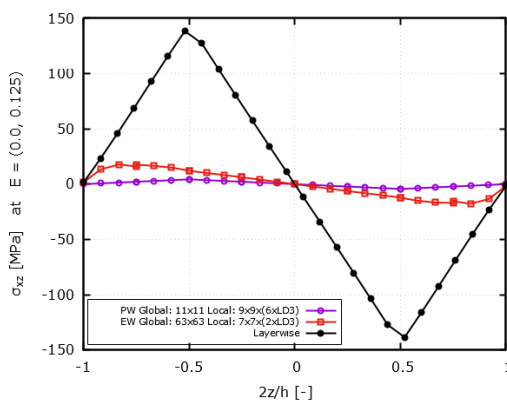
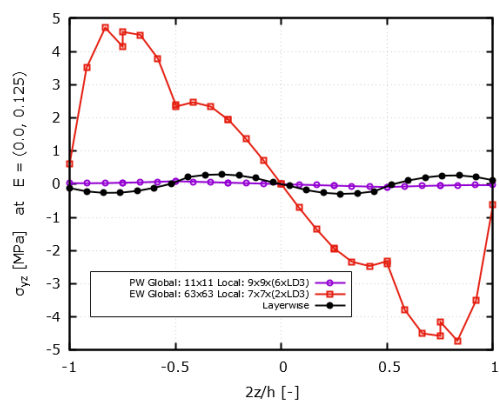


Figure 5.64: PW Stress σ_{yz} at E



5.3.5 Summary of the Thin Plate Stretching

In summary, the thin plate under stretching proved to have a much higher sensitivity to the mesh size than the thin and thick plates under bending. Even though global convergence is found with the u_x and u_y displacements, this does not guarantee good local results, in fact, for all the σ_{ij} stresses computed the best results are found by searching for the combination of global and local meshes concurrently. Nevertheless, the thickness local convergence found that an increasing number of interpolation nodes results in smoother stress curves and more accurate results at layer transitions and boundaries. When it comes to the EW results at point C, it can be said that even though the stress curves do not overlap their respective benchmarks, the global-local curves calculated by the plug-in are still numerically close to them, but the same can not be affirmed of the stresses at the free-edge. Unlike the previous plates, the PW approach does not bring any benefits in terms of numerical results for any of the points under evaluation, C or E . In some cases it provided improvements, but in others, it moved stress curves farther away from the LW benchmark.

The main hypothesis to explain the reason behind the discrepancy in results is the difference in orders of magnitude of the stresses. Generally speaking, any x-axis stress component, meaning σ_{xx} , σ_{xy} , and σ_{xz} is much higher than the other ones σ_{yy} , σ_{yz} , and σ_{zz} , which is expected since the plate is stretched along x . This difference could be introducing numerical errors in the calculations of the global-local plug-in, but nevertheless, further work is necessary to investigate and improve the free-edge calculations of the global-local workflow.

Chapter 6

Conclusions

The objective of this work was to develop a workflow that made the global-local analysis of VAT composite laminates possible. To this extent, an API script was written to automatically build global models through NASTRAN cards. This workflow consisted in the creation of a global model, whose simulation results were input into a local one for the computation of the laminar stresses. The global models were built within the FEMAP environment using two different techniques, the Splines Method and the API script. The first was incapable of correctly modeling the curvilinear paths inherent to VAT laminates, hence the possibility of its implementation was disregarded completely. The latter, which required more time and effort to be developed, was proven to build an accurate global model with the correct tow path approximated for each element. The local model was assembled within the MUL2@GL plug-in of the MUL2 lab of Politecnico di Torino. This in-house tool produced high-order, local, 2D laminate plate, CUF elements that interpolated the vertical displacement fields from the global model with Lagrange Expansions to accurately compute the interlaminar stresses. Finally, this workflow was tested against three different scenarios, a thin plate under bending, a thick plate under bending, and a thin plate under stretching. The first was a basic example to check whether the global model was able to work in combination with the local one. The second tested the limits of the local model by checking whether the workflow was able to work with thick plates. In this example, it was also found that the quality of the local model is very sensitive to the element size. The third and last case intended to test the workflow for the computation of free-edge results. In summary, the global-local workflow was able to replicate the results of the thin plate under bending, especially when the Patch-wise approach was introduced. For this case, both laminar and interlaminar stresses matched with the Layerwise benchmark used for comparison. The stress distributions calculated for the thick plate under bending also matched the ones from its respective benchmark, the results of the work from Demasi. With this example, it was found that the local

element must respect an aspect ratio threshold to produce accurate results, as a mesh that is too refined might output accurate global results, but the computation of the local model deteriorates as its elements become too relatively thick and plate theory begins to fail to lead to numerical errors and results that no longer represent the actual physical behavior of the material. The workflow was finally challenged with a thin plate under stretching. The results at the center of the plate proved to match the Layerwise benchmark, but the computations at the free edge did not as the interlaminar stresses shared little to no resemblance with the LW stress curves. The main explanation for these differences could be that the orders of magnitude of the stress components were very distinct, for instance, σ_{xx} and σ_{xy} were often times 100 times higher than other components such as σ_{yy} and σ_{yz} . These discrepancies could have led to significant numerical errors, which nullified the results. Upon further investigations, it was also found that even the Patch-wise approach that had improved the results of the previous plates was also ineffective as it did not approximate the stress computations to the benchmark. Further work needs to be conducted in order to understand and correctly model the effects of the free edge in VAT laminate plates.

Appendix A

Cubic Interpolations of the Local CUF Element

Regarding the natural reference system on Figure 3.6 the cubic interpolation for the thickness domain z is:

$$\begin{aligned} l_1 &= -\frac{9}{16}z^3 + \frac{9}{16}z^2 + \frac{1}{16}z - \frac{1}{16} \\ l_2 &= +\frac{27}{16}z^3 - \frac{9}{16}z^2 - \frac{27}{16}z + \frac{9}{16} \\ l_3 &= -\frac{27}{16}z^3 - \frac{9}{16}z^2 + \frac{27}{16}z + \frac{9}{16} \\ l_4 &= +\frac{9}{16}z^3 + \frac{9}{16}z^2 - \frac{1}{16}z - \frac{1}{16} \end{aligned} \tag{A.1}$$

Where the indexes l_i refer to the number of the node on z . The in-plane cubic interpolation is based on a 16-node Lagrange polynomial:

$$\begin{aligned}
 L_1 &= \frac{(r-1)(1-9r^2)}{16} \frac{(s-1)(1-9s^2)}{16} \\
 L_2 &= \frac{9(1-r^2)(1-3r)}{16} \frac{(s-1)(1-9s^2)}{16} \\
 L_3 &= \frac{9(1-r^2)(1+3r)}{16} \frac{(s-1)(1-9s^2)}{16} \\
 L_4 &= \frac{(r+1)(9r^2-1)}{16} \frac{(s-1)(1-9s^2)}{16} \\
 L_5 &= \frac{(r+1)(9r^2-1)}{16} \frac{9(1-s^2)(1-3s)}{16} \\
 L_6 &= \frac{(r+1)(9r^2-1)}{16} \frac{9(1-s^2)(1+3s)}{16} \\
 L_7 &= \frac{(r+1)(9r^2-1)}{16} \frac{(s+1)(9s^2-1)}{16} \\
 L_8 &= \frac{9(1-r^2)(1+3r)}{16} \frac{(s+1)(9s^2-1)}{16} \\
 L_9 &= \frac{9(1-r^2)(1+3r)}{16} \frac{(s+1)(9s^2-1)}{16} \\
 L_{10} &= \frac{(r-1)(1-9r^2)}{16} \frac{(s+1)(9s^2-1)}{16} \\
 L_{11} &= \frac{(r-1)(1-9r^2)}{16} \frac{9(1-s^2)(1-3s)}{16} \\
 L_{12} &= \frac{(r-1)(1-9r^2)}{16} \frac{9(1-s^2)(1-3s)}{16} \\
 L_{13} &= \frac{9(1-r^2)(1-3r)}{16} \frac{9(1-s^2)(1-3s)}{16} \\
 L_{14} &= \frac{9(1-r^2)(1+3r)}{16} \frac{9(1-s^2)(1-3s)}{16} \\
 L_{15} &= \frac{9(1-r^2)(1+3r)}{16} \frac{9(1-s^2)(1+3s)}{16} \\
 L_{16} &= \frac{9(1-r^2)(1-3r)}{16} \frac{9(1-s^2)(1+3s)}{16}
 \end{aligned} \tag{A.2}$$

Bibliography

- [1] VantageMarket. «2021 Statistics: U.S. and Global Composite Materials Market Will Surpass \$ 128.82 Billion at 7.52% CAGR Growth: Vantage Market Research (VMR)». In: (2021) (cit. on pp. 1, 2).
- [2] J. Brandt. «THE RESEARCH REQUIREMENTS OF THE TRANSPORT SECTORS TO FACILITATE AN INCREASED USAGE OF COMPOSITE MATERIALS». In: (2004) (cit. on p. 1).
- [3] B. I. Fortune. «Composites Market Size, Share and COVID-19 impact». In: (2020) (cit. on p. 2).
- [4] Eurocontrol. «European Aviation Environmental Report 2019». In: (2019) (cit. on p. 3).
- [5] D. Hull T. W. CLYNE. *An Introduction to Composite Materials. 3. ed.* Cambridge University Press, 2018 (cit. on pp. 3, 4).
- [6] George H. STAAB. *Laminar Composites. 2. ed.* Elsevier B.V, 2015 (cit. on pp. 4, 5).
- [7] A. Martin A. Leissa. «Vibration and buckling of rectangular composite plates with variable fiber spacing». In: (1990) (cit. on p. 5).
- [8] P. Lagace M. DiNardo. «Buckling and postbuckling of laminated composites with ply drop-offs». In: (1989) (cit. on p. 5).
- [9] GUERDAL. *Design and optimisation of laminated composite materials.* Wiley, 1999 (cit. on pp. 5, 21).
- [10] A. Pagani and A.R. Sanchez-Majano. «Stochastic stress analysis and failure onset of variable angle tow laminates affected by spatial fibre variations». In: (2021) (cit. on pp. 6, 15, 22, 32).
- [11] P.M. Weaver Z. Wu. «Buckling analysis and optimisation of variable angle tow composite plates». In: (2012) (cit. on pp. 6, 14).
- [12] R.M.J. Groh G. Zucco. «Mixed shell element for static and buckling analysis of variable angle tow composite plates». In: (2016) (cit. on p. 6).

- [13] G. Raju Z. Wu. «Postbuckling analysis of variable angle tow composite plates». In: (2013) (cit. on p. 6).
- [14] M.A.R. Loja. «Dynamic instability of variable stiffness composite plates». In: (2017) (cit. on p. 6).
- [15] P. M. Weaver B. C. Kim. «Computer aided modelling of variable angle tow composites manufactured by continuous tow shearing». In: (2015) (cit. on p. 6).
- [16] M. Arian Nik A.H. Akbarzadeh. «The role of shear deformation in laminated plates with curvilinear fiber paths and embedded defects». In: (2014) (cit. on p. 6).
- [17] J. H. S. A. Jr Z. Wang. «Reliability-based buckling optimization with an accelerated Kriging metamodel for filament-wound variable angle tow composite cylinders». In: (2020) (cit. on p. 6).
- [18] E. Zappino A. Viglietti. «Free vibration analysis of variable angle-tow composite wing structures». In: (2019) (cit. on p. 7).
- [19] E. Zappino A. Viglietti. «Analysis of variable angle tow composites structures using variable kinematic models». In: (2019) (cit. on p. 7).
- [20] N. Fallahi. «GA Optimization of Variable Angle Tow Composites in Buckling and Free Vibration Analysis through Layerwise Theory». In: (2021) (cit. on p. 7).
- [21] A.H. Akbarzadeh H. Yazdani Sarvestani. «Hygro-thermo-mechanical analysis of fiber-steered composite conical panels». In: (2017) (cit. on p. 7).
- [22] G. Nie X. Chen. «Nonlinear thermal flutter analysis of variable angle tow composite curved panels in supersonic airflow». In: (2021) (cit. on p. 7).
- [23] D.A. Iannotta. «Analisi “global/local” di strutture spaziali dispiegabili in materiale composito». In: (2021) (cit. on pp. 7, 20, 21, 31, 36, 37).
- [24] C. A. Felippa. «INTRODUCTION to FINITE ELEMENT METHODS». In: (2004) (cit. on p. 8).
- [25] N. F. Knight J. B. Ransom. «GLOBAL/LOCAL STRESS ANALYSIS OF COMPOSITE PANELS». In: (1990) (cit. on p. 8).
- [26] G. DOREY. «Carbon fibres and their applications». In: (1987) (cit. on p. 10).
- [27] E. Borzabadi Farahani B. Sobhani Aragha. «Manufacturable insight into modelling and design considerations in fibre-steered composite laminates: State of the art and perspective». In: (2021) (cit. on pp. 11, 13, 15, 16).
- [28] T. Anderson. «Technical Textiles: 6 Methods of Optimizing Carbon Fiber Composites». In: (October 7, 2018) (cit. on p. 12).

- [29] T. Hübner K. Gliesche. «Application of the tailored fibre placement (TFP) process for a local reinforcement on an “open-hole” tension plate from carbon/epoxy laminates». In: (2003) (cit. on p. 12).
- [30] C. Sacco A. Brasington. «Automated fiber placement: A review of history, current technologies, and future paths forward». In: (2021) (cit. on p. 13).
- [31] C. Sacco A. Brasington. «Automated fiber placement: A review of history, current technologies, and future paths forward». In: (2021) (cit. on p. 14).
- [32] C. S. Lopes O. Falco. «Modelling and simulation of tow-drop effects arising from the manufacturing of steered-fibre composites». In: (2017) (cit. on p. 15).
- [33] K. Potter B. C. Kim. «Continuous tow shearing for manufacturing variable angle tow composites». In: (2012) (cit. on pp. 15, 18).
- [34] J. Sjolander P. Hallander. «Forming induced wrinkling of composite laminates with mixed ply material properties; an experimental study». In: (2015) (cit. on p. 16).
- [35] J. Summerscales A. S. Mahmood. «Resin-Rich Volumes (RRV) and the Performance of Fibre-Reinforced Composites: A Review». In: (2022) (cit. on p. 17).
- [36] B. Rasuo Chap. «Impact damage modeling in laminated composite aircraft structures». In: (2012) (cit. on p. 17).
- [37] T. Cavallo. «Component-wise Analysis of Reinforced Thin-walled Metallic and Composite Structures». PhD thesis. Torino: Politecnico di Torino, 2017 (cit. on p. 25).
- [38] T.J.R. HUGHES. *The Finite Element Method: Linear Static and Dynamic Finite Element Analysis*. Dover Publications Inc., 2000 (cit. on p. 30).
- [39] E. CARRERA. *Two-Dimensional Models with Physical Volume/Surface-Based Geometry and Pure Displacement Variables, Cap. 12*. John Wiley Sons, Ltd, 2014 (cit. on p. 37).
- [40] E. Carrera A. Pagani. «Large-deflection and post-buckling analyses of laminated composite beams by Carrera Unified Formulation». In: (2017) (cit. on p. 37).
- [41] L. Demasi. «Hierarchy plate theories for thick and thin composite plates: The generalized unified formulation». In: (2007) (cit. on pp. 38, 50, 59–61, 66).